Chapter 2
Time-Dependent Spectral Shifts in Tryptophan Fluorescence: Bridging Experiments with Molecular Dynamics Simulations

Dmitri Toptygin

Abstract Molecular dynamics (MD) simulations are widely used to model protein motions. Although the time resolution of MD simulations is virtually unlimited, simulated MD is seldom compared with experimental data on the picosecond time scale because few experimental techniques can probe molecular vibrations in the frequency range between 300 MHz and 300 GHz. Time-dependent spectral shift (TDSS, also known as dynamic Stokes shift) in fluorescence emission from solvatochromic dyes has long been used to study relaxation dynamics of polar solvents on the picosecond time scale. This chapter reviews the use of TDSS in connection with protein dynamics. Different methods of calculating TDSS from the non-equilibrium and equilibrium MD are compared and the limits of their applicability are defined. Methods for separating the contributions of water and protein to TDSS are considered. Two relaxation modes of bulk water are described and their effects on the TDSS in proteins are examined. The rates of water relaxation near interfaces and inside protein pockets are evaluated. A method for identifying conformational changes responsible for the TDSS on different time scales is introduced.

Keywords Non-equilibrium protein dynamics • Time-dependent spectral shift • Solvent relaxation • Longitudinal dielectric relaxation • Transverse dielectric relaxation

2.1 Introduction

Empirical forcefields, such as AMBER [1], CHARMM [2], and GROMOS [3], derive the values of the bonded parameters from the experimentally measured vibrational frequencies in the infrared and Raman spectra, which cover the

D. Toptygin (✉)
Department of Biology, Johns Hopkins University, 3400 N. Charles St., Baltimore, MD 21218, USA
e-mail: toptygin@jhu.edu

C.D. Geddes (ed.), *Reviews in Fluorescence 2015*,
DOI 10.1007/978-3-319-24609-3_2

frequency range from 300 GHz to 400 THz. This ensures that simulated molecular dynamics (MD) is always in good agreement with experimental measurements at frequencies between 300 GHz and 400 THz. MD simulations have also been extensively compared to Nuclear Magnetic Resonance (NMR) [4–6], in which the bandwidth of the recorded dynamic signal usually does not exceed 300 MHz. The frequency range from 300 MHz to 300 GHz did not receive as much attention as the frequencies outside of this range. Using the uncertainty principle $\Delta f \Delta t \sim 1/(2\pi)$ where Δf is the bandwidth on the frequency scale and Δt is the pulse width on the time scale, the 300 MHz to 300 GHz frequency range translates to the pulse width range from ~0.5 ps to ~0.5 ns on the time scale. The time scale between ~0.5 ps and ~0.5 ns is here referred to as the "picosecond time scale".

MD simulations are widely used to study protein folding and ligand docking, to estimate thermodynamic stabilities and binding affinities of proteins and other biomolecules [7–10]. Much less often MD simulations are used to study nonequilibrium protein dynamics, such as the dynamics of conformational changes in response to an instantaneous change in one parameter. How well the dynamics obtained from MD simulations agrees with experimental observations on the picosecond time scale is still an open question. The picosecond time scale and the corresponding 300 MHz to 300 GHz frequency range are of critical importance for two reasons. First, all elementary conformational changes in proteins (such as flipping of just one dihedral angle to a different energy minimum) take place on the picosecond time scale. Biologically significant conformational changes, such as folding and unfolding, binding of enzymes to coenzymes and substrates, etc., consist of a multitude of elementary conformational steps and thus take much longer time, but the rates of the big conformational changes are determined by the rates of the elementary conformational steps, which occur on the picosecond time scale.

The second reason why the picosecond time scale is so important has its origin in quantum physics. All existing MD packages are based on the classical (Newtonian) description of nuclear motion, where the rotation of small molecules (like H_2O) about their principal axes of inertia and small groups (like $-CH_3$, $-NH_3^+$, $-CO_2^-$, $-C_6H_5$) about the single bonds connecting these groups to the rest of the biomolecule is not quantized. In quantum mechanics the projection of the angular momentum on the rotation axis can assume only discrete values, which are multiples of $\hbar$ (where $\hbar$ is the Planck's constant divided by 2π), the rotational energies are multiples of $\hbar^2/(2I)$ (where I is the moment of inertia for the rotation about the selected axis), and the rotational transition frequencies are multiples of $\hbar/(4\pi I)$ [11]. Using atomic masses, bond lengths and angles it is not difficult to calculate the fundamental rotational transition frequencies $\hbar/(4\pi I)$ for small groups and molecules: 5.6 GHz for the phenyl group ($-C_6H_5$), 11.5 GHz for the carboxyl group ($-CO_2^-$), 157 GHz for the methyl group ($-CH_3$), 186 GHz for the amino group ($-NH_3^+$), and either 286 GHz or 822 GHz for TIP3P water molecule (depending on the choice of the rotation axis). The biggest difference between classical and quantum mechanics will be observed at frequencies near $\hbar/(4\pi I)$, most of which, as we just saw, fall in the 300 MHz to 300 GHz range.

Classical description of nuclear motion also fails to explain the operation of the ammonia maser [12]. Amplification of microwave radiation by ammonia molecules is due to a transition between two vibrational states [12, 13], which are characterized by different wavefunctions. The most interesting property of these wavefunctions is that the probability density for the normal vibrational coordinate has two equal peaks, i. e., the nitrogen nucleus is on both sides of the plane containing the three hydrogen nuclei [14, 15]. The excited-state wavefunction changes its sign when the nitrogen nucleus crosses the hydrogen plane, whereas the ground-state wavefunction has the same sign on both sides of the plane [14, 15]. Classical description of the nuclear motion cannot handle the case where some (or all) nuclei are delocalized between two (or more) locations at the same time, therefore some of the terms in the interaction energy between molecules with delocalized nuclei are missing in every forcefield that is based on the classical description of nuclear motion. The missing energy terms may play an important role in protein folding. The difference between the classical and quantum description of the nuclear motion is most apparent at frequencies close to those at which masers operate: 24 GHz for the ammonia maser, 22 GHz and 96 GHz for the water maser, etc.. Again, all these frequencies fall between 300 MHz and 300 GHz, where simulated MD has not been adequately tested against experimental data.

Consider the experimental techniques that can be used to study protein dynamics in the 300 MHz to 300 GHz frequency range. Microwave spectroscopy can be used to study protein molecules in vacuum but not in aqueous solution, since liquid water is not transparent in the frequency range between 300 MHz and 300 GHz. The signals measured in dielectric relaxation studies of aqueous protein solutions are overwhelmed by the relaxation of bulk water and contain only a small contribution from the protein molecules, which is largely attributable to the rotation of the protein as a whole. Thus, it is difficult to extract information about vibrational and conformational dynamics in specific protein regions from the dielectric relaxation data. To study the dynamics of elementary conformational changes in proteins and other biomolecules in their native aqueous environment it is necessary to use electromagnetic radiation within the window of transparency of water, which extends over the wavelengths from 200 nm to 900 nm and covers all the visible range, a significant part of the UV range, and a small part of the near-IR range. To convert the spectrum of the electromagnetic signal from the optical range to the low-frequency range ($f < 300$ GHz), and then back from the low-frequency range to the optical range, there must be a nonlinear electro-optical element inside the biomolecule. Any solvatochromic fluorescent dye can play the role of the nonlinear element. Excitation of the solvatochromic dye by a short laser pulse results in a redistribution of its π-orbitals electron density, which, in turn, results in an abrupt change of the magnitude and/or direction of its permanent electric dipole moment. This instantly changes the electrostatic forces acting between the solvatochromic dye and the partial charges on the atoms in its environment. If the system was in the state of equilibrium before the laser pulse, then what we observe after the laser

pulse is known as the nonequilibrium dynamics. As the system relaxes to a new equilibrium, the charged atoms in the vicinity of the solvatochromic dye move in a systematic (non-random) manner, generating a time-variant electric field that acts back on the solvatochromic dye and modulates the energy gap between its ground and excited state via the linear Stark effect. The time variation of the electronic energy gap results in the Time-Dependent Spectral Shift (TDSS) in fluorescence emission.

TDSS has been experimentally observed in the fluorescence of solvatochromic dyes in polar solvents [16–24] and in the fluorescence of solvatochromic fluorophores incorporated in biological macromolecules, such as proteins [25–52] and DNA [53, 54]. While there is a broad consensus that the TDSS in the emission from dyes in polar solvents reflects the relaxation dynamics of the solvent [17], there is still no agreement on the origins of TDSS in biological macromolecules. Some authors attributed experimentally-observed TDSS in proteins to the relaxation of the protein matrix [25–28, 30, 33, 38, 41, 47, 48]. Others argue that the relaxation of the solvent (water) is entirely responsible for TDSS in proteins [32, 35, 36, 39, 42, 46, 49–51]. There are also several reports in which the authors found experimental evidence for contribution from both water and protein matrix to the TDSS [29, 34, 40, 43–45, 52].

One approach that may help to separate the contributions of water and protein matrix to TDSS in proteins is based on the different time scales of these contributions. In bulk water TDSS occurs on the sub-picosecond time scale [18]. TDSS in proteins covers a wide range of time scales, from femtoseconds to at least tens of nanoseconds [25–52]. Abbyad et al. [43] measured TDSS at seven different sites within the same protein. Both sub-picosecond and slower (picosecond and nanosecond) relaxations were found to be contributing to TDSS at every site, however, the sub-picosecond relaxations were found to be dominant at those sites where the fluorophore was in contact with water, and the slower relaxations were found to be dominant at the sites buried deep inside the protein. Based on these findings Abbyad et al. [43] attributed the sub-picosecond TDSS to the relaxation of water, and the slower TDSS to the relaxation of the protein matrix. In accordance with this point of view, in those experiments where the time resolution was much slower than 1 ps, the experimentally observed TDSS would be entirely due to protein relaxation, which is in agreement with the conclusions in most studies where the time resolution was insufficient to detect the relaxation of bulk water [25–27, 33, 38, 41, 48].

A different point of view on the origin of slow TDSS in proteins was expressed by a group of authors [32, 35, 36, 39, 42, 45, 46, 49–52]. According to the latter point of view, the motion of water molecules in the vicinity of the protein is highly constrained, and this “biological water” layer is the sole origin of the slow TDSS in proteins [32, 35, 36, 39]. In later papers it is suggested that the fluctuations of water and protein atoms are coupled and TDSS is attributed the motion of water molecules in the protein hydration layer [42, 45, 46, 49–52]. Thus, there are two diametrically opposite points of view on the origin of slow TDSS in proteins, and

each one has serious implications. If the slow TDSS represents the relaxation of the protein matrix, then it can be used to study the dynamics of elementary conformational changes on the picosecond time scale. However, if the slow TDSS represents the relaxation of "biological water", then it calls for developing a physically viable theory that would explain the properties of this form of H_2O. Unfortunately, experimental evidence alone cannot distinguish the contribution to TDSS due to the relaxation of the protein matrix from that due to the relaxation of the solvent.

MD simulations offer more than one way to separate the contributions of water and protein atoms to TDSS. Numerous MD simulations of TDSS in proteins have been reported [35, 44, 45, 55–62]. In some of these reports the contributions of water and protein atoms to TDSS were separated [45, 56, 57, 59–62], and here the points of view regarding the contributions of water and protein to slow TDSS diverged again. According to Nilsson and Halle [57] water cannot contribute to slow TDSS. According to Golosov and Karplus [60], depending on the location of the solvatochromic fluorophore, TDSS may be due to water, due to protein, or due to both water and protein. In addition, several groups of authors found independently that in those cases where both protein and solvent contribute to the spectral shift, the contributions from protein and water have a negative correlation, i. e., when protein shifts the emission spectrum to the red, water shifts it to the blue and vice versa [56–59, 62]. Halle and Nilsson [63] proposed a simple explanation for the negative correlation based on a dielectric continuum model.

It is likely that the differences in the methods of converting MD trajectories to spectral shifts contributed in part to the differences in the conclusions regarding the relative contributions of protein and water. Non-equilibrium hybrid quantum mechanics - molecular dynamics (QM-MD) simulations were used to calculate TDSS in all papers that came out of the group of Callis [55, 56, 64]. A much faster approach, based on Coulomb's equation, was employed by Hassanali et al. [59] to estimate TDSS from non-equilibrium MD trajectories. A large group of authors used the linear-response method to estimate TDSS [44, 57, 58, 60]. This method makes it possible to estimate TDSS from correlations of random fluctuations in an equilibrium MD trajectory. Some reports describe the application of both the non-equilibrium MD and the linear-response method [45, 61, 62].

This chapter reviews the explicit and implicit assumptions on which different methods of calculating TDSS from the non-equilibrium and equilibrium MD are based and defines the limits of applicability for each method. Also it reviews methods of separating the contributions of water and protein to the TDSS. Two different dielectric relaxation modes of bulk water are considered and their effects on the TDSS of fluorophores in bulk water and those incorporated in protein molecules are examined. The rates of dielectric relaxation of bulk water near interfaces and of isolated water molecules in protein pockets are evaluated. This chapter also describes how one can identify the mode of protein conformational changes responsible for the TDSS on every time scale.

2.2 Relationship Between Spectral Shifts and Electronic Energy Levels

The energies E_0 and E_1 of the singlet electronic states S_0 and S_1 vary with the electric field (Stark effect). Motions of charged and polar chemical groups in the environment of the fluorophore result in a time variation of the energies E_0 and E_1, which will be denoted below as $E_0(t)$ and $E_1(t)$ to emphasize their time dependence. The energy gap $E_1(t)$-$E_0(t)$ defines the frequency ν_{00} of the vibrationless electronic transition (the 0-0 transition):

$$h\nu_{00}(t) = E_1(t) - E_0(t) \tag{2.1}$$

In UV-visible absorption and emission spectra of solvatochromic fluorophores in polar environments, at T ~ 300 K, the vibrational structure cannot be resolved, therefore the value of ν_{00} cannot be determined from experimental data, which makes it impossible to obtain $E_1(t)$-$E_0(t)$ using Eq. (2.1). In most experimental studies the time variation of $E_1(t)$-$E_0(t)$ is estimated from either the peak or the mean frequency in the absorption/emission spectra using one of the following relationships:

$$h\nu_{ab,c}(t) = E_1(t) - E_0(t) + h\nu^{vib}_{ex,c} \tag{2.2}$$

$$h\nu_{ab,\,pk}(t) = E_1(t) - E_0(t) + h\nu^{vib}_{ex,\,pk} \tag{2.3}$$

$$h\nu_{em,c}(t) = E_1(t) - E_0(t) - h\nu^{vib}_{gr,c} \tag{2.4}$$

$$h\nu_{em,\,pk}(t) = E_1(t) - E_0(t) - h\nu^{vib}_{gr,\,pk} \tag{2.5}$$

In these equations h is the Planck constant, ν^{vib} denote vibrational frequencies, ν without a superscript denote frequencies in UV-visible absorption and emission spectra, the subscripts *ab* and *em* refer to absorption and emission, respectively, the subscripts *gr* and *ex* refer to the vibrational frequencies in the ground-state and in the excited-state electronic configuration, respectively, subscript *c* indicates the "center of gravity frequency", i. e., the Franck-Condon factor weighted mean frequency, and the subscript *pk* refers to the peak position in the Franck-Condon factor envelope. The shapes of the Franck-Condon factor envelopes are not identical to the shapes of the absorption and emission spectra, since for transitions with equal Franck-Condon factors the probabilities of emission vary proportionally to ν^3, and the probabilities of absorption vary proportionally to ν^1. To obtain Franck-Condon factor envelopes one has to divide the extinction coefficient spectrum $\varepsilon(\nu)$ by ν and the emitted photon density spectrum $F(\nu)$ by ν^3. Thus, the mean frequencies for the absorption and emission spectra should be calculated as follows:

$$\nu_{ab,c}(t) = \frac{\int_{\nu_1}^{\nu_2} \varepsilon(\nu,t)d\nu}{\int_{\nu_1}^{\nu_2} \varepsilon(\nu,t)\nu^{-1}d\nu} \tag{2.6}$$

$$\nu_{em,c}(t) = \frac{\int_{\nu_3}^{\nu_4} F(\nu,t)\nu^{-2}d\nu}{\int_{\nu_3}^{\nu_4} F(\nu,t)\nu^{-3}d\nu} \tag{2.7}$$

The frequency intervals (ν_1,ν_2) and (ν_3,ν_4) must completely include the absorption band $S_1 \leftarrow S_0$ and the emission band $S_0 \leftarrow S_1$, respectively. The importance of dividing $F(\nu)$ by ν^3 prior to the calculation of the center of gravity has been emphasized in previous work [33, 65], where an expression for emission center of gravity similar to that in Eq. (2.7) was derived.

Equations (2.2, 2.3, 2.4, and 2.5) are similar in one respect: the right-hand side in each of them equals $E_1(t)$-$E_0(t)$ plus a constant term. This means that no matter whether the absorption or emission spectrum is measured and whether the central frequency or the peak frequency is calculated from the instantaneous spectra, essentially the same equation can be used; the only difference is a constant term. A somewhat more complicated situation exists in the case of the time variation of the Stokes shift. Stokes shift is defined as the difference in frequency between the absorption and the emission peak. By subtracting Eq. (2.5) from Eq. (2.3) one can obtain

$$\begin{aligned} h\left[\nu_{ab,\,pk}(t') - \nu_{em,\,pk}(t'')\right] = {} & E_1(t') - E_1(t'') - E_0(t') \\ & + E_0(t'') + h\left[\nu^{vib}_{gr,\,pk} + \nu^{vib}_{ex,\,pk}\right] \end{aligned} \tag{2.8}$$

Here t' and t'' are the instances when the absorption spectrum and the emission spectrum are measured, respectively, and the difference in square brackets on the left-hand side of Eq. (2.8) represents the Stokes shift. If we assume, for instance, that $t' = t''$, then the Stokes shift equals $\nu^{vib}_{gr,\,pk} + \nu^{vib}_{ex,\,pk}$, i. e. the Stokes shift is not time-dependent. The latter appears to be in contradiction with the concept of the time-dependent Stokes shift. However, the condition $t' = t''$ cannot be achieved in reality, since the absorption spectrum can be measured only when the fluorophore is in the ground state, and the emission spectrum can be measured only when it is in the excited state. In time-resolved fluorescence emission experiments the instance of excitation is usually taken for $t = 0$, therefore in Eq. (2.8) $t' = 0$ and $t'' > 0$. In pump-dump-probe experiments [30] one can take the instance of dumping

for $t = 0$, therefore in Eq. (2.8) $t' > 0$ and $t'' = 0$. In general, however, the Stokes shift is a function of two variables rather than one. This makes the terms Time-Dependent Stokes Shift (TDSS) and Dynamic Stokes Shift (DSS) somewhat more confusing than the term Time-Dependent Spectral Shift (TDSS), which represents a function of just one variable. From the second law of thermodynamics it follows that in the case of a homogeneous fluorophore population the TDSS in fluorescence emission is always the Time-Dependent Red Shift (TDRS), and in pump-dump-probe experiments (where the time-resolved absorption spectra after stimulated emission are measured) the TDSS is always a Time-Dependent Blue Shift (TDBS).

2.3 Effect of the Electric Field on the Electronic Energy Levels

Quantum-mechanical perturbation theory has long been used to describe the Stark effect in atoms and molecules [11]. Here we use the perturbation theory to derive a simple equation relating the energy gap $E_1(t)$-$E_0(t)$ that enters in each of Eqs. (2.1, 2.2, 2.3, 2.4, and 2.5) to the local electric field acting on the fluorophore. Within the framework of the perturbation theory, the Hamiltonian operator $\hat{H}$ of the fluorophore (in the fixed-nuclei approximation) must be represented as a sum of an unperturbed Hamiltonian $\hat{H}(0)$and a perturbation $\hat{V}$,

$$\hat{H} = \hat{H}(0) + \hat{V} \tag{2.9}$$

The theory of the Stark effect is usually applied to an atom or a molecule in vacuum. In this case the Hamiltonian operator in the absence of the external electric field is taken for $\hat{H}^{(0)}$, and $\hat{V}$ describes the additional potential energy of interaction between the electrons and the external electric field. It is shown below (see Sect. 2.4, "Nonlinear Stark Effect") that this approach may yield inaccurate results in the case of a solvatochromic fluorophore in a polar environment, especially if the fluorophore possesses two close electronic energy levels. Here $\hat{H}^{(0)}$is defined as the Hamiltonian operator for the fluorophore in a uniform electric field [66] $\mathbf{E}^{(0)}$, and $\hat{V}$ is defined as the additional potential energy due to the difference between the actual electric field (which does not have to be uniform) and $\mathbf{E}^{(0)}$. If $\mathbf{E}^{(0)}$ does not differ too much from the mean [67] electric field in the environment of the fluorophore, then the errors resulting from the use of the method described here will be insignificant, see Sect. 2.4, "Nonlinear Stark Effect". The perturbed energies E_n of the two lowest singlet electronic levels ($n = 0,1$) can be expressed in the form suggested by Landau [11]:

$$E_n = E_n^{(0)} + E_n^{(1)} + E_n^{(2)} + \ldots \tag{2.10}$$

$$E_n^{(1)} = V_{nn} \tag{2.11}$$

$$E_n^{(2)} = \sum_{m \neq n} \frac{|V_{mn}|^2}{E_n^{(0)} - E_m^{(0)}} \tag{2.12}$$

Here $E_n{}^{(0)}$ denote the unperturbed energy levels, i. e. the eigenvalues of the unperturbed Hamiltonian $\hat{H}^{(0)}$, $E_n{}^{(1)}$ denote the first-order corrections, $E_n{}^{(2)}$ denote the second-order corrections, and V_{nn} and V_{mn} represent the diagonal and off-diagonal matrix elements of the perturbation Hamiltonian $\hat{V}$. In a uniform electric field $\mathbf{E}$ the matrix elements of the perturbation Hamiltonian can be conveniently expressed in terms of the matrix elements of the electric dipole operator:

$$V_{mn} = -\boldsymbol{\mu}_{mn}^{(0)} \cdot (\mathbf{E} - \mathbf{E}^{(0)}) \tag{2.13}$$

Here $\cdot$ denotes a scalar product of two vectors. Vectors $\boldsymbol{\mu}_{mn}^{(0)}$ are the matrix elements of the electric dipole operator, defined on the basis set of eigenfunctions $\Psi_n{}^{(0)}$ of the Hamiltonian $\hat{H}^{(0)}$, which represents the fluorophore in the uniform electric field $\mathbf{E}^{(0)}$.

The electric field acting on a fluorophore in a polar environment is generated mostly by charged and polar groups in close proximity to the fluorophore; this field is not expected to be uniform. For our purposes it is more convenient to describe the non-uniform electric field by its scalar potential ϕ rather than by the vector $\mathbf{E}$. The uniform electric field $\mathbf{E}^{(0)}$ corresponds to the following potential,

$$\phi^{(0)}(\mathbf{r}) = -\ \mathbf{r} \cdot \mathbf{E}^{(0)} \tag{2.14}$$

Thus, the deviation of the electric field from the uniform field is described by the potential

$$\delta\phi(\mathbf{r}) = \phi(\mathbf{r}) - \phi^{(0)}(\mathbf{r}) = \phi(\mathbf{r}) + \mathbf{r} \cdot \mathbf{E}^{(0)} \tag{2.15}$$

The perturbation Hamiltonian is defined as follows,

$$\hat{V} = \sum_k q_k \delta\phi(\mathbf{r}_k) \tag{2.16}$$

Here the summation is carried out over all charged elementary particles, including electrons and nuclei, q_k is the charge of the particle k and $\mathbf{r}_k$ is the radius-vector describing its coordinates. Matrix elements of this perturbation Hamiltonian are calculated as usual [11], which involves integration over the coordinates of all electrons, but not over the coordinates of the nuclei, because here we are using the

fixed-nuclei approximation. For the diagonal matrix elements the result of this integration can be reduced to the following expression:

$$V_{nn} = \sum_j Q_{jn}^{(0)} \delta\phi(\mathbf{r}_j) \tag{2.17}$$

Here the summation is carried out over all atoms of the fluorophore, $\mathbf{r}_j$ is the radius-vector of the center of atom j, and $Q_{jn}{}^{(0)}$ is Mulliken atomic charge [68] on atom j when the fluorophore is in the state S_n. The partial charges $Q_{jn}{}^{(0)}$ must be calculated using eigenfunctions $\Psi_n{}^{(0)}$ of the Hamiltonian $\hat{H}(0)$, which represents the fluorophore in the uniform electric field $\mathbf{E}^{(0)}$. In transition from Eq. (2.16) to Eq. (2.17) we have assumed that the electron density can be attributed to individual atoms as suggested by Mulliken [68] and that the electron density attributed to each atom is symmetrically distributed about the atom's center (spherical symmetry). The latter assumption is accurate only for the inner-shell electrons; the distribution of valence electrons is not spherically symmetrical. However, the errors associated with deviations from the spherical symmetry are smaller than the errors associated with using the electric dipole approximation in a non-uniform electric field, therefore Eq. (2.17) is likely to give more accurate results than Eq. (2.13).

From Eqs. (2.10, 2.11, and 2.17) follows the first-order estimate for the energy E_n:

$$E_n = E_n^{(0)} + \sum_j Q_{jn}^{(0)} \mathbf{r}_j \cdot \mathbf{E}^{(0)} + \sum_j Q_{jn}^{(0)} \phi(\mathbf{r}_j) \tag{2.18}$$

or

$$E_n = G_n^{(0)} + \sum_j Q_{jn}^{(0)} \phi(\mathbf{r}_j) \tag{2.19}$$

where the constant energies G_n are defined as follows

$$G_n^{(0)} = E_n^{(0)} + \sum_j Q_{jn}^{(0)} \mathbf{r}_j \cdot \mathbf{E}^{(0)} \tag{2.20}$$

Now E_n from Eq. (2.19) can be substituted for E_1 and E_0 in each of the Eqs. (2.2, 2.3, 2.4, and 2.5). The following equation was obtained from Eq. (2.5), however, similar results can be obtained from Eqs. (2.2), (2.3), or (2.4):

$$h\nu_{em,\,pk}(t) = G_1^{(0)} - G_0^{(0)} - h\nu_{gr,\,pk}^{vib} + \sum_j \left(Q_{j1}^{(0)} - Q_{j0}^{(0)}\right)\phi(\mathbf{r}_j, t) \tag{2.21}$$

Note, that $Q_{j1}^{(0)} - Q_{j0}^{(0)}$ represents the difference between the partial atomic charge on atom j in the excited and in the ground state. This difference will be denoted $\Delta Q_j^{(0)}$:

$$\Delta Q_j^{(0)} = Q_{j1}^{(0)} - Q_{j0}^{(0)} \tag{2.22}$$

Using this new notation we can rewrite the sum on the right-hand side of Eq. (2.21) in the form

$$\Delta E(t) = \sum_j \Delta Q_j^{(0)} \phi(\mathbf{r}_j, t) \tag{2.23}$$

Replacing the first three constant terms on the right hand side of Eq. (2.21) with a new constant $h\nu_0$ and the last term with $\Delta E(t)$ from Eq. (2.23) yields

$$h\nu(t) = h\nu_0 + \Delta E(t) \tag{2.24}$$

Here we have dropped the subscripts *em* and *pk* on the left-hand side because Eq. (2.24) equally applies to absorption and emission spectra and it also equally applies to peak frequencies and center-of-gravity frequencies; only the definition of the constant term $h\nu_0$ is different in these cases.

2.4 Nonlinear Stark Effect

In transition from Eqs. (2.10, 2.11, 2.17) to Eq. (2.18) we have omitted the second-order and higher correction terms that appear on the right-hand side of Eq. (2.10). A sum of the terms that have been omitted represents the error arising from the use of Eq. (2.23). This error will be considered now.

Equation (2.12) gives the second-order correction term, which is usually the most significant of the terms that have been omitted. The off-diagonal matrix elements V_{mn} in Eq. (2.12) cannot be expressed in terms of Mulliken partial atomic charges as we did it with the diagonal matrix elements in Eq. (2.17). This means that in estimating the errors we will have to limit ourselves to the case of a uniform electric field, where Eq. (2.13) can be used. Substituting V_{mn} from Eq. (2.13) into Eq. (2.12) yields

$$E_n^{(2)} = \sum_{m \neq n} \frac{|\boldsymbol{\mu}_{mn}^{(0)} \cdot (\mathbf{E} - \mathbf{E}^{(0)})|^2}{E_n^{(0)} - E_m^{(0)}} \tag{2.25}$$

Equation (2.25) explicitly shows that the second-order correction term $E_n^{(2)}$ is quadratic in $\mathbf{E} - \mathbf{E}^{(0)}$. Furthermore, it can be shown that every other term $E_n^{(k)}$ also varies with the field as the k-th power of $\mathbf{E} - \mathbf{E}^{(0)}$. Thus, the series in Eq. (2.10)

represents an expansion of the energy E_n in powers of $\mathbf{E} - \mathbf{E}^{(0)}$. This series has a finite convergence domain. The convergence domain is limited by a convergence boundary. When the point $\mathbf{E}^{(0)}$, in the neighborhood of which the series expansion is made, is at the convergence boundary, the convergence is lost completely. This will be used to identify the convergence boundaries for the expansion in Eq. (2.10). If $E_m = E_n$ for some $m \neq n$, then one of the denominators in the sum in Eq. (2.25) equals zero. This is also true for all correction terms $E_n^{(k)}$ with $k \geq 2$. The set of all points where the condition $E_m = E_n$ is met for at least one $m \neq n$, represents the convergence boundary. Since we are only interested in the series expansions for E_0 and E_1, the convergence domain is limited by the boundaries $E_m = E_0$ and $E_m = E_1$. For most fluorophores, the ground state is separated from the lowest electronically-excited state by a large energy gap, therefore the condition $E_m = E_0$ is not likely to be reached in a realistic experimental setting. On the contrary, the condition $E_m = E_1$ is commonly achieved when two excited electronic states "cross" each other. For example, 3-methylindole, which plays the role of the fluorophore in tryptophan (Trp), has two excited electronic configurations commonly referred to as ${}^1L_a$ and ${}^1L_b$ [69]. In vacuum ${}^1L_b$ is the lowest excited state and ${}^1L_a$ is higher in energy [64]. In a polar solvent the lowest excited state is ${}^1L_a$ and ${}^1L_b$ has a greater energy [64]. This means that in some electric field of intermediate strength between that in a polar environment and in vacuum the energies E_1 and E_2 must be equal, and this defines the convergence boundary. If we choose $\mathbf{E}^{(0)}$ on one side of that boundary, then the series expansion of E_1 will diverge on the other side of that boundary. This means that if we choose $\mathbf{E}^{(0)} = \mathbf{0}$, which corresponds to vacuum, then the series in Eq. (2.10) is going to diverge for the fluorophore in a polar environment. However, if we choose $\mathbf{E}^{(0)}$ equal to the Onsager reaction field in a polar solvent, then the series in Eq. (2.10) are going to diverge in vacuum.

In those cases where the first-order estimate from Eq. (2.23) is used for $\Delta E(t)$, the question of convergence becomes irrelevant, however, the question of accuracy still comes down to the correct choice of $\mathbf{E}^{(0)}$. Since the second- and higher-order correction terms $E_n^{(k)}$ vary with the field as the k-th power of $\mathbf{E} - \mathbf{E}^{(0)}$, minimizing the absolute value of the difference $\mathbf{E} - \mathbf{E}^{(0)}$ is the obvious way of reducing the errors. To achieve this goal, the value of $\mathbf{E}^{(0)}$ should be chosen close to the mean [67] value of $\mathbf{E}$ experienced by the fluorophore in the specific environment where the TDSS is studied. This choice of $\mathbf{E}^{(0)}$ will ensure the most accurate values of the differential partial charges $\Delta Q_j^{(0)}$ and it will ultimately result in accurate first-order estimates of TDSS.

2.5 Hybrid QM-MD Versus Classical MD

Quantum mechanical (QM) calculations provide the most accurate way of calculating $\Delta E(t)$ for a fluorophore in an electric field. Hybrid QM-MD simulations of TDSS in proteins and peptides have been reported by the group of Callis [55, 56, 70]. Hybrid QM-MD simulations usually cover only a short period of time, from

2 ps [55] to 30 ps [56] for proteins, and up to 60 ps for small peptides[70]. In those cases where several nanoseconds of TDSS must be calculated, the use of QM-MD simulations is not desirable because of their slow speed. This has encouraged many authors [44, 45, 57, 59–62] to use a faster method of calculating $\Delta E(t)$ from MD trajectories, which is based on Eq. (2.26) or its equivalent,

$$\Delta E(t) = \frac{1}{4\pi\varepsilon_0} \sum_i \sum_j \frac{Q_i \ \Delta Q_j^{(0)}}{|\mathbf{r}_j(t) - \mathbf{r}_i(t)|} \tag{2.26}$$

Here ε_0 is the dielectric permittivity of vacuum, index i counts all atoms except those that belong to the fluorophore, Q_i is the partial electric charge on atom i, $\mathbf{r}_i(t)$ is the radius-vector of this atom at time t, index j counts only the fluorophore atoms, $\Delta Q_j^{(0)}$ is defined in Eq. (2.22), $\mathbf{r}_j(t)$ is the radius-vector of atom j at time t, and $|\mathbf{a} - \mathbf{b}|$ denotes the magnitude of the difference between the vectors $\mathbf{a}$ and $\mathbf{b}$.

Although Eq. (2.26) may be obvious to those who use it, it is important to understand how it is obtained and what are the errors associated with the use of this equation. Here Eq. (2.26) is obtained by substituting into Eq. (2.23) the following expression for the electric potential $\phi(\mathbf{r},t)$:

$$\phi(\mathbf{r}, t) = \frac{1}{4\pi\varepsilon_0} \sum_i \frac{Q_i}{|\mathbf{r} - \mathbf{r}_i(t)|} \tag{2.27}$$

Equation (2.27) represents the electrostatic potential generated by the partial electric charges of all atoms except those that belong to the fluorophore. The same electrostatic potential is used in hybrid QM-MD simulations, therefore any differences in accuracy between the hybrid QM-MD simulations and the faster method based on Eq. (2.26) must arise from Eq. (2.23) and not from Eq. (2.27). Equation (2.23) was obtained from the first-order quantum-mechanical perturbation theory [11]. The use of the perturbation theory is inevitable when we deal with a quantum system containing more than two elementary particles: analytical solution of the Schrodinger equation exists only for the hydrogen atom, while for any atom with more than one electron as well as for any molecule the use of the perturbation theory is unavoidable. The QM portion of the hybrid QM-MD simulations is entirely based on the perturbation theory. Thus, the errors associated with the faster method of calculating $\Delta E(t)$ do not result from the use of the perturbation theory, but they result from the use of the first-order perturbation theory. The errors are equal to the sum of the higher-order correction terms that were originally included in Eq. (2.10), but were then dropped. These terms are discussed in Sect. 2.4, "Nonlinear Stark Effect", where it is concluded that in order to minimize the omitted higher-order correction terms one has to use the differential partial charges $\Delta Q_j^{(0)}$ corresponding to the fluorophore in the electric field $\mathbf{E}^{(0)}$ that closely resembles the mean local field acting on the fluorophore. The mean local field can be obtained from a hybrid QM-MD simulation, which does not have to be very long. Thus, the best way to evaluate ${Q_{j1}}^{(0)}$, ${Q_{j0}}^{(0)}$, and $\Delta Q_j^{(0)}$ is to run a short hybrid

QM-MD simulation and to average the instantaneous partial charges on the fluorophore atoms over a time period of several picoseconds. Callis and co-workers [56, 64] ran QM-MD simulations (using CHARMM forcefield) for 3-methylindole in ^1L_a excited state in a drop of 1100 explicit TIP3 waters and averaged the charges over the last 4 ps of the trajectory. Then all $Q_{j1}^{(0)}$, $Q_{j0}^{(0)}$, and $\Delta Q_j^{(0)}$ were scaled by a factor of 0.80 [56], which was necessary to obtain the best match between the simulated and experimental ΔE values. It is still unclear why the calculated ΔE values were not accurate without the scale factor. From Eq. (2.26) it follows that the scaling of all $\Delta Q_j^{(0)}$ by some factor has the same effect on ΔE as the scaling of all Q_i by the same factor, therefore one possible explanation is that in CHARMM the partial charges Q_i on protein and solvent atoms are exaggerated on average by a factor of 1/(0.80). The other possible explanation is that CHARMM is not a polarizable forcefield; using a polrizable forcefield would probably decrease the electric field on average by a factor of 0.80, which would make the calculated ΔE values closer to the experimental ones. The charges $Q_{j1}^{(0)}$, $Q_{j0}^{(0)}$, and $\Delta Q_j^{(0)}$ that were originally obtained by Callis and co-workers [56, 64] and then used by others to calculate TDSS from MD trajectories [62] are given in Table 2.1. This appears to be the best set of charges to be substituted in Eq. (2.26) in combination with the partial charges Q_i from the CHARMM forcefiled. The use of $\Delta Q_j^{(0)}$ from Table 2.1 and Eq. (2.26) makes possible to accurately calculate TDSS from a non-equilibrium MD trajectory without the use of hybrid QM-MD simulations.

2.6 Direct-Response Versus Linear-Response Method

Non-equilibrium MD is commonly triggered by switching the partial charges of the fluorophore atoms from $Q_{j0}^{(0)}$ to $Q_{j1}^{(0)}$ at $t = 0$. TDSS is then calculated using Eq. (2.26) directly from a non-equilibrium MD trajectory; this approach will be called the direct-response method to distinguish it from the linear-response method. TDSS calculated using the direct-response method from just one MD trajectory is overwhelmed by random noise, therefore averaging over about 100 trajectories is usually necessary. An alternative approach, known as the linear-response method, makes it possible to obtain the same information from the autocorrelation of random fluctuations in just one very long equilibrium trajectory. The method is described below.

Consider some interaction with the energy $\Delta E(t)$ that can be instantaneously turned on. For example, Coulombic interaction between the additional charges $\Delta Q_j^{(0)}$ on fluorophore atoms and the common partial charges of other atoms instantaneously turns on when the fluorophore jumps from the ground state to the excited state. Equation (2.26) gives the energy of this interaction. According to the fluctuation-dissipation theorem, in the linear-response approximation, the ensemble average response $\langle \Delta E(t) \rangle$ averaged over an infinite number of non-equilibrium

Table 2.1 Trp side chain atom charges in units of positive electron charge e. Reprinted with permission from Ref. [62], copyright 2010 American Chemical Society

Trp atom	$Q_{j0}^{(0)}$	$Q_{j1}^{(0)}$	$\Delta Q_j^{(0)}$
CB	−0.003	+0.004	+0.007
HB1	+0.013	+0.017	+0.004
HB2	+0.016	+0.015	−0.001
CG	−0.046	+0.184	+0.230
CD1	+0.011	+0.122	+0.111
HD1	+0.030	+0.047	+0.017
NE1	−0.130	+0.017	+0.147
HE1	+0.125	+0.132	+0.007
CE2	+0.052	+0.082	+0.030
CD2	−0.009	−0.087	−0.078
CE3	−0.027	−0.214	−0.187
HE3	+0.027	+0.028	+0.001
CZ3	−0.033	−0.077	−0.044
HZ3	+0.005	−0.003	−0.008
CZ2	−0.039	−0.243	−0.204
HZ2	+0.017	+0.021	+0.004
CH2	−0.026	−0.063	−0.037
HH2	+0.017	+0.018	+0.001

trajectories, in which the interaction is turned on at t=0, is connected to the autocorrelation function $C(t)$ defined below by a simple relation:

$$\langle \Delta E(t) \rangle - \langle \Delta E(\infty) \rangle = \beta \; C(t) \tag{2.28}$$

Here β is the inverse temperature, $\beta = 1/(k_B T_A)$, where k_B is Boltzmann constant and T_A is absolute temperature. The autocorrelation function $C(t)$ can be defined either as ensemble average, i. e. the average over infinite number of trajectories, or as a time average over one infinitely long trajectory. We will use the second approach, because in practice the autocorrelation function is always obtained from one trajectory [44, 45, 57, 58, 60–62]. Time-averaged $C(t)$ is defined as the limit at $T \to \infty$ of the autocorrelation function obtained from a finite-length trajectory,

$$C(t) = \lim_{T \to \infty} C_T(t) \tag{2.29}$$

Here $C_T(t)$ is calculated from a trajectory of length T; it is defined as follows:

$$C_T(t) = \frac{1}{T-t} \int_0^{T-t} \left[\Delta E(t') - \overline{\Delta E_T} \right] \left[\Delta E(t'+t) - \overline{\Delta E_T} \right] dt' \tag{2.30}$$

$$\overline{\Delta E_T} = \frac{1}{T}\int_0^T \Delta E(t')dt' \tag{2.31}$$

$\Delta E(t')$ must be calculated from an equilibrium trajectory, i. e. the interaction should not be turned on or turned off during the MD simulation that generates $\Delta E(t')$ to be used in Eqs. (2.30 and 2.31).

The results obtained using the linear-response method contain both random errors and systematic errors. The random errors originate from substituting $C_T(t)$ instead of $C(t)$ into Eq. (2.28). For a short trajectory the difference between $C_T(t)$ and $C(t)$ can be substantial, which can easily lead to false interpretations. The most common artifacts in $C_T(t)$ resulting from averaging over a finite-length trajectory are illustrated in Fig. 2.1.

The random noise in panel 1A of Fig. 2.1 is a sum of the random fluctuations in 16 noise-driven damped harmonic oscillators with different frequencies and different damping ratios (Langevin dynamics) [62]. This random noise visually resembles $\Delta E(t)$ from a real MD simulation, yet, computing this random noise is millions of times faster than a real MD simulation for a real protein, which makes it easy to study the evolution of $C_T(t)$ up to $T = 10{,}000$ ns. Panel 1A shows only the first 10 ns of $\Delta E(t)$, however, the "trajectory" was actually generated all the way up to $t = 10{,}000$ ns. In panel 1B of Fig. 2.1 the black line depicts $C_{10\text{ns}}(t)$, calculated from the part of the trajectory in panel 1A. The red line depicts $C_{10000\text{ns}}(t)$, which is practically identical to $C(t)$, since it was established that the increase in T from 5000 to 10000 ns produces no visible changes in $C_T(t)$ [62]. The difference between $C_{10\text{ns}}(t)$ and $C_{10000\text{ns}}(t)$ is the low-frequency noise, which is a common artifact associated with the use of the linear-response method. Theoretically, it should be possible to decrease the amplitude of the low-frequency noise to a desired level, however, in practice this would require a very long MD trajectory, since the amplitude of the noise in $C_T(t)$ decreases as $T^{-½}$. The low-frequency noise, also known as pink noise, is potentially more dangerous than the white noise in direct-response TDSS, because the low-frequency noise is not subjectively perceived as noise.

The noise pattern in panel 1A of Fig. 2.1 resembles near-equilibrium atomic fluctuations in a protein that does not change its conformation at all. If the entire protein or just one side chain in close proximity to the fluorophore jumps between two discrete isomers, then the noise pattern may look like the ones shown in panels 2A or 3A. $\Delta E(t)$ in panels 2A and 3A were generated using a random switch that jumps between two discrete levels [62]. The switch in panel 2A spends equal times (on average) in both states; the average time between jumps for this switch equals 5 ns. The switch in panel 3A spends 90 % of time in the lower energy state and 10 % in the upper energy state, with the residence times of 0.33 ns for the upper energy state and 3 ns for the lower energy state. The random noise from the 16 damped harmonic oscillators was also added to the signals depicted in panels 2A and 3A. $\Delta E(t)$ curves were generated for a total of 10000 ns in all cases.

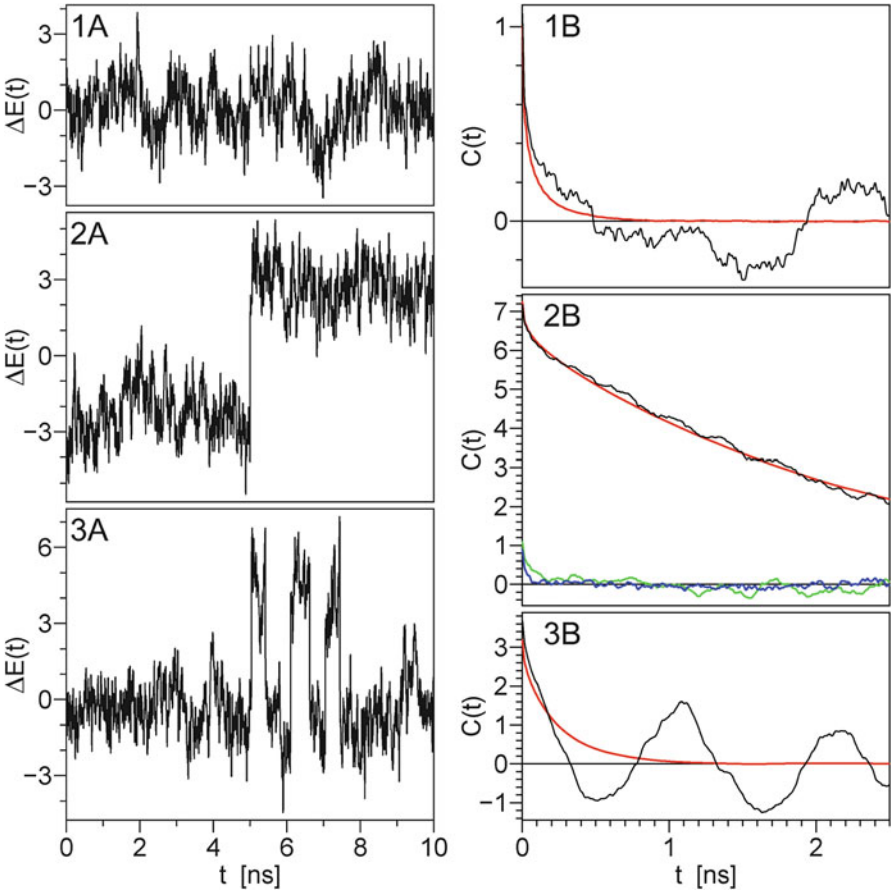

Fig. 2.1 Random noise patterns (panels **1A, 2A, 3A**) and corresponding autocorrelation functions $C_T(t)$ (panels **1B, 2B, 3B**). The *black* line in each #B panels represents $C_{10ns}(t)$ calculated from the 10 ns trajectory in the corresponding #A panel using Eqs. (2.30 and 2.31). The *red* line represents $C_{10000ns}(t)$ calculated from the 10000 ns trajectory generated by the same random process as the 10 ns trajectory in the corresponding #A panel. The *green* and the *blue lines* in panel **2B** depicts $C_{5ns}(t)$ calculated from for the first 5 ns and from the last 5 ns of the trajectory in panel **2A**, respectively. Reprinted with permission from Ref. [62], copyright 2010 American Chemical Society

Panel 2A of Fig. 2.1 shows a selected 10 ns window during which the protein spent the first 5 ns as isomer 1 (low ΔE) and the following 5 ns as isomer 2 (high ΔE). The autocorrelation $C_{10ns}(t)$ calculated from the selected window (black line in panel 2B) and the autocorrelation $C_{10000ns}(t)$ calculated from the full trajectory (red line in panel 2B) are close to each other, and this is for a good reason: the average times the protein spends as isomer 1 or isomer 2 equal 5 ns, and during the selected 10 ns window it spent exactly 5 ns as isomer 1 and 5 ns as isomer 2. Random switching between isomers makes a large contribution to $C(t)$ and it is solely responsible for the difference between the red line in panel 2B and the red line in

panel 1B. This switching increases the full amplitude of the autocorrelation function from 1.0 in panel 1B to 7.2 in panel 2B. It also increases the correlation time from less than 0.5 ns in panel 1B to more than 2.5 ns in panel 2B. Thus, switching between two (or more) isomers could be the main source of the slow TDSS observed experimentally on the time scales of nanoseconds or even tens of nanoseconds [25–27, 33, 38, 41, 48]. The green and blue lines in panel 2B depict $C_{5\text{ns}}(t)$ calculated from for the first 5 ns (during which only isomer 1 was present) and from the last 5 ns (during which only isomer 2 was present) of the trajectory in panel 2A. Since there were no transitions between the isomers during the time windows used to calculate either $C_{5\text{ns}}(t)$, the slow TDSS is not observed in this case. An example of splitting MD trajectory in two parts can be found in the work of Li et al. [45, 61], who separately analyzed the trajectories for the isomers 1 and 2 using the linear-response method. No nanosecond-scale relaxation was found in this work [45, 61]. This example clearly shows how insufficient trajectory length T can radically alter the results obtained using the linear-response method.

The example shown in panels 3A and 3B illustrates a possible but unlikely situation. During the 10 ns window selected for panel 3A the protein jumped from the low ΔE state (isomer 1) to the high ΔE state (isomer 2) and back three times in a row. $\Delta E(t)$ does not behave like this during every 10 ns window, thus, the piece of trajectory shown in panel 3A is atypical. This explains the big difference between the black and the red line in panel 3B. The black line represents $C_{10\text{ns}}(t)$ calculated from the selected 10 ns window. The red line represents $C_{10000\text{ns}}(t)$ calculated from the full trajectory, and it closely approximates $C(t)$. While the red line approaches the zero level aperiodically, the black line shows oscillations characteristic of an underdamped oscillator. Golosov and Karplus [60] found the underdamped behavior in just one of the eleven linear-response MD trajectories they simulated. This can be the case of a real underdamped oscillator or the case where the low-frequency noise resembles the behavior of an underdamped oscillator, similar to that shown in panels 3A and 3B. To find out which is the case, one would have to generate a much longer linear-response MD trajectory.

The results obtained using the linear-response method may also contain systematic errors. The systematic errors have their origin in deviations from linearity. Equation (2.28) is valid only in the linear-response approximation, therefore in the case where $\beta|\Delta E|>1$, i. e., $|\Delta E|>k_B T_A$, the use of Eq. (2.28) can result in significant systematic errors. The systematic errors will be further investigated here using a very simple model system, which consists of just one TIP3P water molecule in a uniform electric field that is turned on at $t=0$. The orientation of the water molecule is described here using Euler angles (ϕ,θ,ψ) [71]. The Z' axis of the molecular frame is chosen parallel to the permanent electric dipole moment $\boldsymbol{\mu}$ of the water molecule, and the Z axis of the laboratory frame is chosen parallel to the electric field $\mathbf{E}$. With this choice of axes, the interaction energy depends on only one Euler angle:

$$\Delta E(t) = -\boldsymbol{\mu}\cdot\mathbf{E} = -|\boldsymbol{\mu}||\mathbf{E}|\cos\theta \tag{2.32}$$

Using the fact that in the absence of the electric field the orientation of the water molecule is random, and therefore $\langle\cos^2\theta\rangle$=1/3, we can calculate the value of $C(t)$ for t=0:

$$C(0) = \langle \Delta E^2(t)\rangle = |\boldsymbol{\mu}|^2|\mathbf{E}|^2\langle\cos^2\theta\rangle = \frac{1}{3}|\boldsymbol{\mu}|^2|\mathbf{E}|^2 \tag{2.33}$$

According to the linear-response method,

$$\langle \Delta E(0)\rangle - \langle \Delta E(\infty)\rangle = \beta C(0) = \frac{1}{3}\beta|\boldsymbol{\mu}|^2|\mathbf{E}|^2 \tag{2.34}$$

Taking into account that $\langle \Delta E(0)\rangle = 0$ and $\langle \Delta E(\infty)\rangle = |\boldsymbol{\mu}||\mathbf{E}|\langle\cos\theta\rangle$, one can obtain the following expression for the equilibrium value of $\langle\cos\theta\rangle$ in the presence of the electric field:

$$\langle\cos\theta\rangle = \frac{1}{3}\beta|\boldsymbol{\mu}||\mathbf{E}| \tag{2.35}$$

The estimate in Eq. (2.35) is based on the linear-response approximation, therefore it is accurate in weak electric fields only. A general expression for the equilibrium value of the first-rank order parameter $\langle\cos\theta\rangle$ in the electric field of any strength can be obtained using the equilibrium orientational distribution of the molecule, which is essentially a Boltzmann distribution in Euler angles:

$$d^3P(\phi,\theta,\psi) = A\exp(\beta|\boldsymbol{\mu}||\mathbf{E}|\cos\theta)\, d\phi\, \sin\theta d\theta\, d\psi \tag{2.36}$$

The constant A in Eq. (2.36) must be chosen so that the integral over all orientations equals unity. Multiplying the distribution in Eq. (2.36) by $\cos\theta$ and integrating over all orientations yields

$$\langle\cos\theta\rangle = \coth(\beta|\boldsymbol{\mu}||\mathbf{E}|) - (\beta|\boldsymbol{\mu}||\mathbf{E}|)^{-1} \tag{2.37}$$

In Fig. 2.2 the estimate obtained using the linear-response method, Eq. (2.35), is depicted by the red line, and the value from Eq. (2.37), which is accurate at any level of the electric field, is depicted by the blue line. The curves in Fig. 2.2 were calculated using $\beta = 1/(k_B \times 300\ \text{K})$, which corresponds to the temperature of 300 K, and $|\boldsymbol{\mu}| = 7.829{\cdot}10^{-30}$C·m, which is the magnitude of the permanent electric dipole moment of a TIP3P water molecule. The relative deviation of the linear-response estimate from the actual value reaches 10 % at the electric field strength of 7 MV/cm. The additional excited-state charges $\Delta Q_j^{(0)}$ on the Trp side chain (see Table 2.1) generate an electric field of 7 MV/cm magnitude at distances up to 8.5 Å from the center of the fluorophore. Thus, if the distance between the center of the indole moiety and the center of at least one water molecule is less than 8.5 Å, then the amplitude of the TDSS obtained using the linear-response method is likely to be

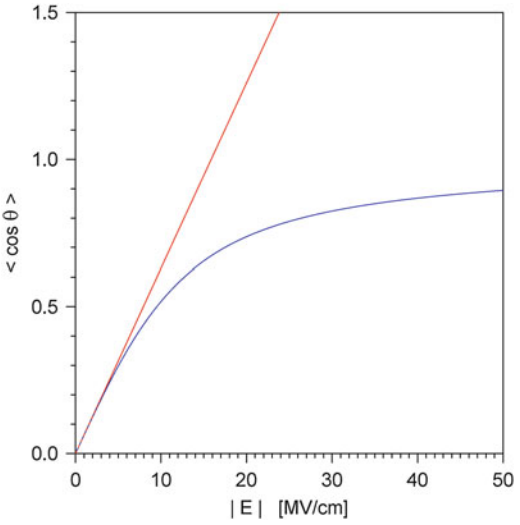

Fig. 2.2 The first-rank order parameter $\langle \cos\theta \rangle$ for a TIP3P water molecule in a uniform electric field **E**. *Red line*: the estimate obtained using the linear-response method, Eq. (2.35). *Blue line*: the exact value from Eq. (2.37). The curves were calculated for 300 K temperature and $7.829 \cdot 10^{-30}$C·m dipole moment. Reprinted with permission from Ref. [62], copyright 2010 American Chemical Society

overestimated. A water molecule in van der Waals contact with the Trp side chain may experience electric fields up to 50 MV/cm; in electric fields of this magnitude the estimate obtained using the linear-response method is 3.5-fold greater than one obtained using the direct-response method. An overestimated amplitude is always accompanied by a distorted shape of the TDSS, therefore re-normalization does not solve the problem, it just makes it more difficult to be acknowledged. Maroncelli and Fleming [72] questioned the validity of the linear-response method when they discovered that in linear-response MD simulations the solvation response to a charge jump in ST2 water does not vary linearly with the magnitude of the charge jump. Comparing the theoretical estimates in Eqs. (2.35) and (2.37) makes it possible to determine in advance whether the results of a future linear-response MD simulation will be valid or not.

2.7 Separation of Contributions from Different Motions

A trivial method for separating the protein and solvent contributions to TDSS is based on splitting the summation over the index i in Eq. (2.26) into two partial sums. The first partial sum covers the range of i that corresponds to protein atoms; this partial sum represents the protein contribution to TDSS. The second partial sum involves only those i values that correspond to solvent atoms and represents the solvent contribution to TDSS. This method of separating the protein and solvent contributions to TDSS was used several times [45, 56, 57, 59, 60]. The main drawback of this method is that it attributes the TDSS resulting from the motion of the fluorophore itself in part to the protein and in part to the solvent. In rigid proteins where the fluorophore is tightly packed in the protein core and cannot

rotate relative to the protein this drawback is unimportant and the use of the trivial separation method is justifiable. On the other hand, if the protein is not rigid and/or the fluorophore is on the surface, then the use of the trivial separation method may result in significant errors. A method allowing the separation of contributions from the motion of the fluorophore itself, from the motion of other protein atoms, and from the motion of solvent atoms was recently proposed [62]. A description of this method is given below.

According to Eq. (2.23) the spectral shift depends on the radius-vectors $\mathbf{r}_j$ of the fluorophore atoms and also on the electric potential $\phi(\mathbf{r},t)$ generated by the partial charges of all atoms except those of the fluorophore. Thus, the motion of the fluorophore as well as the motion of the surrounding atoms contribute to the spectral shift. To be able to tell which atoms moved and how far, we will have to choose a reference frame. It makes little sense to consider atomic motions in the laboratory frame, since in this frame the rotation and translation of the protein as a whole results in much greater atomic displacements than those relative atomic motions that actually produce TDSS. It makes even less sense to use the reference frame attached to a small atomic group (e. g., one side chain) of the protein molecule, or to a water molecule. The only reasonable choice is to attach the reference frame to the protein molecule. Since the molecule is flexible, the question how this can be practically accomplished is not trivial. An algorithm (based on successive iterations) for defining the reference frame attached to the protein is described in Ref. [62]. Coordinate transformations between the laboratory reference frame and that attached to the protein molecule are described by the following equations:

$$\mathbf{r}^{lab} = \mathbf{R}\mathbf{r}^{mol} + \mathbf{u} \tag{2.38}$$

$$\mathbf{r}^{mol} = \mathbf{R}^T\left(\mathbf{r}^{lab} - \mathbf{u}\right) \tag{2.39}$$

Here $\mathbf{r}^{lab}$ denotes the column vector of three Cartesian coordinates x^{lab}, y^{lab}, z^{lab} in the laboratory reference frame; these are the coordinates used in MD simulations. Likewise $\mathbf{r}^{mol}$ denotes the column vector of three Cartesian coordinates x^{mol}, y^{mol}, z^{mol} in the reference frame attached to the protein molecule. Throughout this chapter equations containing radius-vectors $\mathbf{r}$ without superscripts are valid regardless of the choice of the reference frame; for example Eq. (2.26) is valid both in the laboratory and in the molecular reference frame. If radius-vectors from more than one reference frame appear in the same equation, then each radius-vector is provided with a superscript to identify its reference frame, as in Eqs. (2.38 and 2.39). $\mathbf{R}$ denotes a 3×3 rotation matrix of the special orthogonal group SO(3); its transpose $\mathbf{R}^T$ is equal to its inverse. $\mathbf{u}$ is the translation vector, which describes the position of the origin of the molecular reference frame in the laboratory reference frame. The rotation and translation of the protein molecule results in the time variation of the matrix $\mathbf{R}$ and vector $\mathbf{u}$.

For every protein atom n (including fluorophore atoms) the vector of mean equilibrium coordinates $\langle \mathbf{r}_n{}^{mol} \rangle$ is defined as the ensemble averages of $\mathbf{r}_n{}^{mol}$ at

long times after excitation. In practice one can average $\mathbf{r}_n^{mol}$ over all MD trajectories and also over a time period that starts after the bulk of the TDSS is over and continues to the end of the trajectory. Note, that averaging is carried out on the coordinates of protein atoms only and in the reference frame attached to the protein; it makes no sense to average any Cartesian coordinates in the laboratory reference frame or to average the coordinates of solvent atoms in the protein reference frame.

Using the mean coordinate vectors $\langle \mathbf{r}_j^{mol} \rangle$ for the fluorophore atoms it is possible to split the energy $\Delta E(t)$ in Eq. (2.23) into the part $\Delta E_f(t)$ that varies due to the motion of the fluorophore itself and the part $\Delta E_e(t)$ that varies due to the changes in the electric field:

$$\Delta E(t) = \Delta E_f(t) + \Delta E_e(t) \tag{2.40}$$

$$\Delta E_f(t) = \sum_j \Delta Q_j^{(0)} \left[\phi\left(\mathbf{r}_j^{mol}, t \right) - \phi\left(\left\langle \mathbf{r}_j^{mol} \right\rangle, t \right) \right] \tag{2.41}$$

$$\Delta E_e(t) = \sum_j \Delta Q_j^{(0)} \phi\left(\left\langle \mathbf{r}_j^{mol} \right\rangle, t \right) \tag{2.42}$$

Here $\Delta Q_j^{(0)}$ is the charge difference defined in Eq. (2.22) and ϕ is the electric potential defined in Eq. (2.27). If the fluorophore does not move in the reference frame attached to the protein, then all the differences in square brackets on the right-hand side of Eq. (2.41) equal zero, and therefore $\Delta E_f(t)$ also equals zero. On the other hand, in the hypothetical situation where all protein atoms except those of the fluorophore itself and all water atoms are fixed in the reference frame attached to the protein, the potentials $\phi(\langle \mathbf{r}_j^{mol} \rangle, t)$ are time-invariant, and therefore $\Delta E_e(t)$ is also time-invariant. In other words, without the motion of the fluorophore there is no time variation in $\Delta E_f(t)$, and without the motions of other atoms there is no time variation in $\Delta E_e(t)$. This justifies treating $\Delta E_f(t)$ as the contribution of the fluorophore atoms and $\Delta E_e(t)$ as the contribution of non-fluorophore protein atoms and solvent atoms.

To split $\Delta E_e(t)$ further into the contributions of protein and solvent atoms, the electric potentials $\phi(\langle \mathbf{r}_j^{mol} \rangle, t)$ that appear in Eq. (2.42) must be expressed explicitly in terms of the coordinates of these atoms,

$$\phi(\langle \mathbf{r}_j^{mol} \rangle, t) = \frac{1}{4\pi\varepsilon_0} \sum_i \frac{Q_i}{|\mathbf{r}_i^{mol}(t) - \langle \mathbf{r}_j^{mol} \rangle|} \tag{2.43}$$

Here index i counts all atoms except those that belong to the fluorophore, Q_i is the partial charge on atom i, and $\mathbf{r}_i^{mol}$ the coordinate vector for this atom. The time variation of $\phi(\langle \mathbf{r}_j^{mol} \rangle, t)$ results only from the time variation of $\mathbf{r}_i^{mol}$, since the partial atomic charges Q_i and the mean coordinates $\langle \mathbf{r}_j^{mol} \rangle$ are time-invariant. The contribution of one non-fluorophore atom i to $\Delta E_e(t)$ and also to $\Delta E(t)$ can be obtained by taking just one term from the sum in Eq. (2.43) and substituting it in Eq. (2.42),

$$\Delta E_i(t) = \frac{1}{4\pi\varepsilon_0} \sum_j \frac{\Delta Q_j^{(0)} Q_i}{\left| \mathbf{r}_i^{mol}(t) - \left\langle \mathbf{r}_j^{mol} \right\rangle \right|} \tag{2.44}$$

The contribution of one fluorophore atom j to $\Delta E_f(t)$ and also to $\Delta E(t)$ can be obtained by taking just one term from the sum in Eq. (2.41). The solvent contribution can be determined by summing up $\Delta E_i(t)$ from Eq. (2.44) over all water atoms. The contribution of the protein can be determined by summing up $\Delta E_i(t)$ from Eq. (2.44) over all non-fluorophore protein atoms; in the case where the fluorophore (e. g., tryptophan) is considered to be a part of the protein it is also necessary to add $\Delta E_f(t)$ from Eq. (2.41) to the sum. The protein contribution, water contribution, and contributions of individual atoms must be then averaged over all nonequilibrium trajectories (ensemble averaging).

2.8 Dielectric Relaxation of Bulk Solvent

Dielectric relaxation of the solvent usually has a significant contribution to the TDSS of fluorophores in proteins. Dielectric relaxation of polar solvents occurs on multiple time scales [73]. The Debye model of dielectric relaxation in polar liquids contains only one characteristic time constant τ_D, which is commonly called the Debye relaxation time [17, 73–76]. An exponential term of the form $\exp(-t/\tau_D)$ is directly observed in the time variation of the electric displacement **D** after a jump in the electric field **E** in the form of Heaviside step function $\theta(t)$ [76], as shown in the top panel of Fig. 2.3. However, if the step-function jump is applied to the electric displacement **D**, then the relaxation of the electric field **E** does not contain the term $\exp(-t/\tau_D)$. Instead, it contains a faster exponential term $\exp(-t/\tau_L)$ [76], as shown in the bottom panel of Fig. 2.3. The relationship between τ_L and τ_D is well known [17, 73–76],

$$\tau_L = \frac{\varepsilon_\infty}{\varepsilon_S} \tau_D \tag{2.45}$$

In Eq. (2.45) ε_S is the static (low-frequency) dielectric permittivity of the solvent, ε_∞ is the high-frequency dielectric permittivity of the solvent, τ_L is the longitudinal relaxation time, and τ_D is the transverse relaxation time and also the Debye relaxation time. The terms "transverse" and "longitudinal" are relevant in the case of a continuous homogeneous polar liquid without borders or foreign objects. Using Helmholtz decomposition the dielectric polarization density **P** can be separated into two independent parts: (i) the longitudinal part, for which the divergence of **P** is non-zero ($\nabla \cdot \mathbf{P} \neq 0$) and the curl of **P** equals the zero vector ($\nabla \times \mathbf{P} = \mathbf{0}$), and (ii) the transverse part, for which the divergence of **P** equals zero ($\nabla \cdot \mathbf{P} = 0$) and the curl of **P** is not equal to the zero vector ($\nabla \times \mathbf{P} \neq 0$) [73]. If the dielectric response is described by the Debye model, then both the longitudinal and

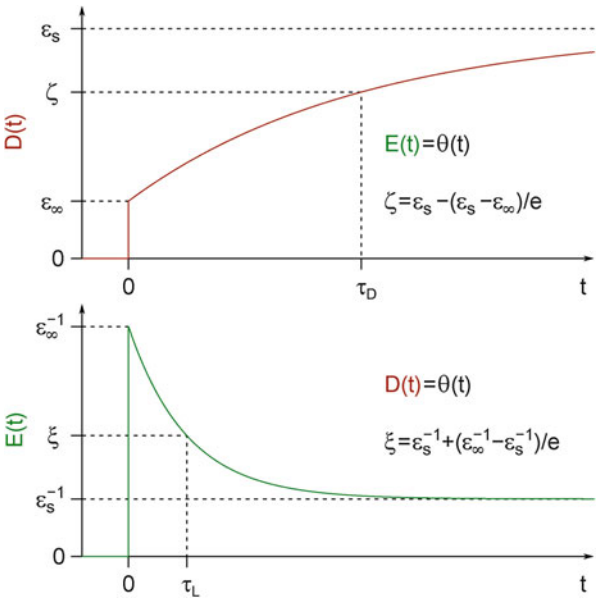

Fig. 2.3 Graphical definitions of the transverse relaxation time τ_D (*top panel*) and longitudinal relaxation time τ_L (*bottom panel*). $\mathbf{E}(t)$ is the electric field, $\mathbf{D}(t)$ is the electric displacement, and $\theta(t)$ is Heaviside step function. Adapted with permission from Ref. [62], copyright 2010 American Chemical Society

the transverse component relax exponentially, but with different relaxation times τ_L and τ_D [73, 76].

The dielectric polarization near a spherical ion immersed in a continuous homogeneous polar solvent consists of the longitudinal part only, therefore a step-function jump in the charge of the ion would induce an exponential relaxation process with the characteristic time τ_L. Such a charge jump contradicts the principle of electric charge conservation, therefore it cannot be achieved in practice. A step-function jump in the electric dipole moment is practically achievable; it occurs when a solvatochromic fluorophore jumps from the ground state to the excited state. Maroncelli and Fleming [74] have shown that for a point-dipole centered inside a spherical cavity a step-function jump in the dipole moment induces a relaxation process containing a single exponential term $\exp(-t/\tau_F)$, where [74, 75]

$$\tau_F = \frac{2\varepsilon_\infty + \varepsilon_C}{2\varepsilon_S + \varepsilon_C}\tau_D \tag{2.46}$$

In Eq. (2.46) ε_C is the dielectric permittivity of the spherical cavity, which is intended to represent fluorophore polarizability. From Eqs. (2.45 and 2.46) it follows that $\varepsilon_C = 0$ results in $\tau_F = \tau_L$, while $\varepsilon_C = \infty$ results in $\tau_F = \tau_D$. According to realistic estimates [17, 74, 75], for spherical fluorophores in polar solvents τ_F is only slightly greater than τ_L, while τ_D is much greater then both τ_L and τ_F.

The above example with a dipole jump in a spherical cavity shows that the observed dielectric relaxation cannot be always separated in two parts with the characteristic relaxation times τ_L and τ_D. Complete separation of the transverse and longitudinal polarization components can be accomplished only in the absence of

borders and foreign objects (such as the spherical cavity in the above example). In the case of a parallel-plate capacitor the concepts "transverse" and "longitudinal" become completely irrelevant. The electric field **E** between the plates of such a capacitor is uniform, and so is the dielectric polarization density **P**, therefore the divergence of **P** equals zero ($\nabla \cdot \mathbf{P} = 0$) and the curl of **P** equals the zero vector ($\nabla \times \mathbf{P} = \mathbf{0}$), which fits neither the definition of longitudinal polarization nor the definition of transverse polarization [73]. Yet, with a parallel-plate capacitor one can observe both relaxation times τ_L and τ_D. If a step-function jump is applied to the voltage across the capacitor, then the charge on each plate of the capacitor will change with time as $\mathbf{D}(t)$ in the top panel of Fig. 2.3. However, if a step-function jump is applied to the charge on the plates of the same capacitor, then the voltage across the capacitor will change with time as $\mathbf{E}(t)$ in the bottom panel of Fig. 2.3.

In all previous examples the relaxation curve contained only one exponential term, which could be $\exp(-t/\tau_L)$, or $\exp(-t/\tau_F)$, or $\exp(-t/\tau_D)$. Now the question is whether two or more exponential terms can be observed simultaneously in a relaxation curve if the solvent is described by the Debye relaxation model. One physical structure in which both $\exp(-t/\tau_L)$ and $\exp(-t/\tau_D)$ can be observed simultaneously is depicted in the top panel of Fig. 2.4. A layer of a non-polar solid dielectric (such as polyethylene or diamond), shown by the yellow color in the top panel of Fig. 2.4, is immersed in a polar liquid (such as water), shown by the blue color. A narrow cylindrical channel, whose diameter is much smaller than the thickness of the layer, is drilled through the solid dielectric and is also filled with the polar liquid. The whole structure is placed between the plates of a parallel-plate capacitor (shown by black color, with the + and − labels) and a step-function jump is applied to the charge on the plates of this capacitor. This creates a step-function jump in $\mathbf{D}_1$ (the electric displacement in the polar liquid). Since $\mathbf{D}_1$ and $\mathbf{D}_2$ are both normal to the interface between the two dielectrics, $\mathbf{D}_1 = \mathbf{D}_2$, and therefore there is also a step-function jump in $\mathbf{D}_2$ (the electric displacement in the non-polar dielectric). For the non-polar dielectric the static dielectric constant and the high-frequency dielectric constant is the same quantity, which will be denoted ε_{NP}. The relationship between the electric field and the electric displacement in the non-polar dielectric is instantaneous, i. e. $\mathbf{D}_2 = \varepsilon_{NP}\mathbf{E}_2$, which results in a step-function jump in $\mathbf{E}_2$ (the electric field in the non-polar dielectric). Since $\mathbf{E}_2$ and $\mathbf{E}_3$ are both parallel to the walls of the cylindrical channel, $\mathbf{E}_2 = \mathbf{E}_3$, and therefore there is also a step-function jump in $\mathbf{E}_3$ (the electric field in the polar liquid inside the channel). A step-function jump in the electric field in the polar liquid results in a relaxation process that contains the exponential term $\exp(-t/\tau_D)$. The relaxation of the polar liquid outside the channel will result in the term $\exp(-t/\tau_L)$. Therefore, both τ_L and τ_D can be observed at the same time in one dielectric relaxation curve.

Using a conformal transformation the planar structure shown in the top panel of Fig. 2.4. can be transformed to a near-spherical structure shown in the left bottom panel of Fig. 2.4. Since conformal transformations preserve the solutions of Maxwell-Lorentz equations, the dielectric relaxation curves observed with the structures in the bottom left panel and in the top panel of Fig. 2.4 are identical; exponential terms with both τ_L and τ_D will be observed in the dielectric relaxation

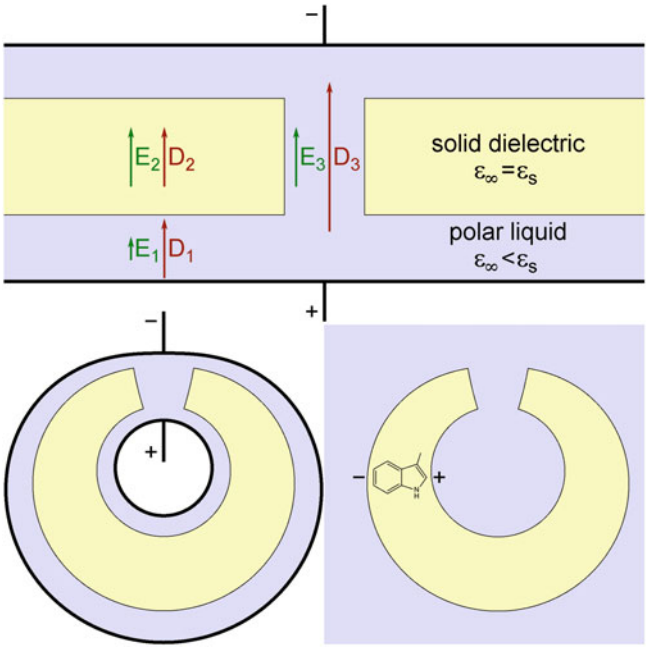

Fig. 2.4 Examples of simple structures in which both $\exp(-t/\tau_D)$ and $\exp(-t/\tau_L)$ are present in the dielectric relaxation curve (*top panel* and *left bottom panel*) or in the TDSS (*right bottom panel*)

curve using either of these structures. Furthermore, the size of the structure shown in the bottom left panel of Fig. 2.4 is not important, it can be reduced to that of a protein. In the next step we remove the capacitor plates (shown by black color, with the + and − labels) and replace them by a solvatochromic fluorophore, such as the sidechain of tryptophan. The result is shown in the bottom right panel of Fig. 2.4. In the TDSS of the fluorophore shown in the bottom right panel one will observe two exponential terms, one with τ_L, and one with τ_D.

Generally speaking, it should be also possible to observe two exponential terms, one with a τ close to τ_L, and one with a τ close to τ_D, in an experiment where a solvatochromic fluorophore is embedded in a non-polar dielectric of irregular shape and immersed in a polar liquid. The hydrophobic core of a protein can play the role of the non-polar dielectric, however, an irregular shape made of polyethylene or diamond can play this role equally well. An exponential term with a τ close to τ_D is expected only if the non-polar structure contains at least one narrow channel filled with the polar solvent and if the cross-section of the channel is significantly smaller than the surface area of each of the two cavities that are connected by the channel (one of these cavities can be the outside solvent). If the structure contains no internal solvent pockets and no channels, then no slow relaxation terms with characteristic times close to τ_D will be observed, but there can still be more than one exponential term with τ between τ_L and τ_D. When the shape of the dielectric

structure approaches a perfect sphere, the number of exponential terms in the TDSS reduces to one with $\tau = \tau_F$ given by Eq. (2.46).

The value of τ_D for liquid water at 25 °C equals 8.27 ps [77]. This value, as well as the experimental values [77] of $\varepsilon_S = 78.36$ and $\varepsilon_\infty = 5.2$ can be substituted in Eq. (2.45), which yields a 550 fs estimate for the longitudinal relaxation time τ_L. Experimental TDSS of coumarin 343 in bulk water was reported to contain two close exponentials with $\tau = 126$ fs and $\tau = 880$ fs [18], with the amplitude-weighted mean τ_F of 606 fs. This, as expected, is not far from $\tau_L = 550$ fs. According to Eq. (2.46) the value of τ_F increases with the polarizability of the fluorophore, therefore τ_F values as high as 1 ps are expected in the case of highly polarizable fluorophores, such as 3-methylindole, in water. Solvent relaxation times longer than about 1 ps are not expected for solvatochromic dyes immersed directly in water. Using the example of Fig. 2.4. it was demonstrated here that if the solvatochromic dye is embedded in an irregular-shaped nonpolar dielectric (or in a protein) that is immersed in water, then a relaxation time close to $\tau_D = 8.27$ ps can contribute to TDSS in some cases. This relaxation time represents a different relaxation mode of the solvent and has nothing to do with the biological aspects of the irregular-shaped nonpolar dielectric. The addition of free ions like K^+ or Cl^- to water can further increase the value of τ_D. The addition of organic hydrogen-bonding co-solvents, such as ethanol, ethylene glycol, glycerol, etc. results in non-exponential solvent relaxation with some very slow components that can be much slower than τ_D of pure H_2O.

2.9 Relaxation of Water Molecules Near Protein Surface and Inside Protein

In the previous section we considered the relaxation of the bulk solvent, where it was possible to treat the solvent as a continuous dielectric. Now we will consider the solvent at the level of individual molecules. A rigid solvent molecule can participate in two kinds of motion: the translational motion and the rotational motion. First of all, we will show that the contribution from the translational motion of a solvent molecule to dielectric relaxation and to TDSS is always insignificant in incompressible liquids. The contribution of one solvent molecule to the energy of a capacitor in a dielectric relaxation experiment or to $\Delta E(t)$ in a TDSS measurement equals $-\boldsymbol{\mu}_S \cdot \mathbf{E}$, where $\boldsymbol{\mu}_S$ is the electric dipole moment of the solvent molecule and $\mathbf{E}$ is the electric field. In a dielectric relaxation experiment $\mathbf{E}$ is generated by the charges on the capacitor plates, and in a TDSS experiment it is generated by the charges $\Delta Q_j^{(0)}$ defined in Eq. (2.22). In a uniform electric field (the case of dielectric relaxation) the energy $-\boldsymbol{\mu}_S \cdot \mathbf{E}$ is independent of the location of the solvent molecule, therefore the translational motion has zero contribution to the dielectric relaxation curve. The electric field generated by $\Delta Q_j^{(0)}$ is not uniform, and it can be decomposed into the dipole, quadrupole, octupole, and higher multipole terms.

The significance of these terms decreases in the order in which they are listed here. For a rough estimate we will keep only the most significant dipole term and disregard the smaller terms. The dipole moment of the fluorophore is

$$\boldsymbol{\mu}_F = \sum_j \Delta Q_j^{(0)} \mathbf{r}_j \tag{2.47}$$

and it generates the electric field

$$\mathbf{E} = \frac{1}{4\pi\varepsilon_0}\left(\frac{3(\boldsymbol{\mu}_F \cdot \mathbf{r})\mathbf{r}}{|\mathbf{r}|^5} - \frac{\boldsymbol{\mu}_F}{|\mathbf{r}|^3}\right) \tag{2.48}$$

where $\mathbf{r}$ is now measured from the center of the fluorophore. For a rough estimate we will assume that the shape of the fluorophore is spherical and that the dipole $\boldsymbol{\mu}_\mathrm{F}$ is pointing in the direction from the "south pole" to the "north pole". A solvent molecule located near either pole of the fluorophore sphere has the largest possible contribution to TDSS, which equals $-\xi\cos\theta$, where $\xi = |\boldsymbol{\mu}_\mathrm{S}||\boldsymbol{\mu}_\mathrm{F}|/(2\pi\varepsilon_0 R^3)$, θ is the angle between $\boldsymbol{\mu}_\mathrm{S}$ and $\boldsymbol{\mu}_\mathrm{F}$, and R is the sum of the van der Waals radii of the fluorophore and the solvent. If the solvent molecule moves from the pole to the equator, then its contribution to TDSS changes from $-\xi\cos\theta$ to $+(\xi/2)\cos\theta$, i. e. 1.5-fold, whereas if it just rotates in place from $\theta = 0°$ to $\theta = 180°$, then its contribution to TDSS changes from $-\xi$ to $+\xi$, i. e. twofold. To move from the pole to the equator the solvent molecule would have to travel the distance of $\pi R/2$, which would require several exchanges of places between the solvent molecule under consideration and other solvent molecules. The orientation of two molecules cannot be preserved when they switch places in a liquid, therefore the likelihood of the event that a solvent molecule would travel all the way from the pole to the equator without changing its orientation is negligible, and so is the contribution of the translational motion to the TDSS.

The exchange between a water molecule hydrogen-bonded to protein surface and a free water molecule represents a special case of the translational motion. This motion does not contribute to TDSS either, because (as a result of the hydrogen bonding) after such exchange the second water molecule will be in the same orientation in which the first one was before the exchange, while the orientation of the free molecule (the second one before the exchange, the first one after the exchange) changes much faster than the rate of exchange between the two molecules. While the contribution to the TDSS from each molecule changes significantly during their exchange, the net contribution to TDSS from both molecules equals that of the rotational relaxation of the free molecule. This basically means that the residence times of the molecules bound to protein surfaces are not involved in the exponential terms observed in the TDSS.

Once we have established that only the rotational motion of solvent molecules contributes to TDSS, it is necessary to explain how this one type of motion can be responsible for both the longitudinal relaxation mode of the bulk solvent with the

relaxation time τ_L and the transverse relaxation mode with the relaxation time τ_D. During the relaxation process the electric field generated by the relaxing solvent molecules superimposes on the external electric field (which triggers the relaxation in the first place), and this represents a feedback mechanism. In the case of the longitudinal relaxation the feedback is negative, and this is what makes the relaxation dynamics faster. In the case of the transverse relaxation the feedback is zero (the net electric field **E** does not change during the transverse relaxation, which was emphasized in Fig. 2.3 and in the corresponding discussion). Thus, τ_D can be considered the intrinsic relaxation time of a solvent molecule in the absence of the feedback. Using Eq. (2.35) and the expression for the dipole-dipole interaction energy it is not difficult to derive the following expression for the feedback coefficient between two solvent molecules in a weak uniform electric field:

$$f_{mn} = \frac{|\boldsymbol{\mu}_S|^2}{4\pi\varepsilon_0 k_B T_A R_{mn}^3}\left(\cos^2\theta_{mn} - \frac{1}{3}\right) \tag{2.49}$$

Here $|\boldsymbol{\mu}_S|$ is the magnitude of the electric dipole moment of each solvent molecule, ε_0 is dielectric permittivity of vacuum, k_B is Boltzmann constant, T_A is absolute temperature, R_{mn} is the distance between the centers of the solvent molecules m and n, θ_{mn} is the angle between the electric field **E** and the line connecting the centers of the molecules m and n. The additional electric field acting on molecule n from the molecule m equals $f_{mn}\mathbf{E}$. The feedback coefficient is positive for $0^\circ < \theta_{mn} < 54.7^\circ$ and $125.3^\circ < \theta_{mn} < 180^\circ$; it is negative for $54.7^\circ < \theta_{mn} < 125.3^\circ$. Averaging of the feedback from Eq. (2.49) over all solvent molecules in the bulk solvent results in a large negative feedback, which reduces the relaxation time from τ_D to τ_L. If the solvent molecule is at the planar interface between the bulk solvent and a nonpolar solid dielectric, then exactly one half of the positive feedback and exactly one half of the negative feedback disappears regardless of the angle between **E** and the plane of the interface, which results in a relaxation time close to $2\tau_L$. This shows that near a planar interface with a non-hydrogen-binding substance the longitudinal relaxation time roughly doubles, and this has nothing to do with the biological aspects of the nonpolar dielectric.

Now consider a linear chain of water molecules connecting a reaction center in the protein core with external water [78, 79]. For the electric field component parallel to the linear chain the feedback coefficients between all water molecules are positive, which may significantly slow down the relaxation dynamics. A solvent relaxation component significantly slower than τ_D may be observed in this case.

The relaxation time for an isolated solvent molecule in the protein core is expected to be comparable to τ_D if the molecule has about as much rotational freedom as one in the bulk solvent. If the solvent molecule is directly adjacent to a charged chemical group, such as $-NH_3^+$ or $-CO_2^-$, then its dipole moment is always aligned with the strong electric field from the charged group; the contribution from this water molecule to TDSS is expected to be small in amplitude and

very fast (a few femtoseconds), like that of the stoichiometric water in ionic crystals, e. g. $CuSO_4{\cdot}5H_2O$.

2.10 Separation of Relaxation Modes by Their Time Scales

In Sect. 2.5 it was shown how the total TDSS energy $\Delta E(t)$ can be calculated from nonequilibrium MD trajectories. In Sect. 2.7 it was shown how the fluorophore contribution $\Delta E_f(t)$, the protein contribution $\Delta E_p(t)$, and the solvent contribution $\Delta E_s(t)$ can be separated. The total TDSS and the contributions must be then ensemble-averaged over a large number of nonequilibrium MD trajectories. The next step is the separation of the relaxation modes by their time scales. This can be accomplished by globally fitting the total TDSS as well as the contributions to it from the fluorophore, solvent and protein by the following model function,

$$\Delta E_c(t) = \alpha_{c,0} + \sum_{n=1}^{N_{\exp}} \alpha_{c,n} \exp[-\max(t,0)/\tau_n] \tag{2.50}$$

In Eq. (2.50) c represents the name of the component (f for fluorophore contribution, s for solvent, p for protein, and blank for the total effect), n is the number of the exponential term, $\alpha_{c,n}$ is the corresponding amplitude, and τ_n is the corresponding relaxation time. The values of all fitting parameters $\alpha_{c,n}$ and τ_n must be determined simultaneously in the course of a global weighted nonlinear least square minimization. Due to the well known negative correlation [56–59, 62, 63] between the protein and the solvent contribution to TDSS it is easy to miss some of the relaxation components when only the total TDSS is fitted. Separately fitting the curves $\Delta E(t)$, $\Delta E_f(t)$, $\Delta E_p(t)$, and $\Delta E_s(t)$ results in four different sets of relaxation times τ_n that cannot be reconciled after the fitting.

Global fitting of the component TDSS curves calculated from 100 nonequilibrium MD trajectories for the tryptophan fluorophore in GB1 protein has been described [62]. The ensemble-averaged component TDSS is presented in Figs. 2.5 and 2.6. A minimum of five exponential terms in Eq. (2.50) was required for an adequate fit to the data. The values of the five relaxation times τ_n resulting in the best global fit to the data are: $\tau_1 = 36.1 \pm 1.6$ fs, $\tau_2 = 384 \pm 26$ fs, $\tau_3 = 5.63 \pm 0.33$ ps, $\tau_4 = 131 \pm 5$ ps, and $\tau_5 = 2.58 \pm 1.06$ ns. The amplitudes associated with the five exponential terms and their decomposition into the contributions from the solvent, protein, and fluorophore are shown in Fig. 2.7 in the form of a histogram.

The histogram in Fig. 2.7 shows how much energy protein and solvent contribute to each relaxation mode, but it says nothing about the mechanical character of the motions associated with these modes. To reveal the mechanical nature of the relaxation modes the following operations have been carried out [62]. All protein internal coordinates (bond lengths, bond angles, dihedral angles) and also all

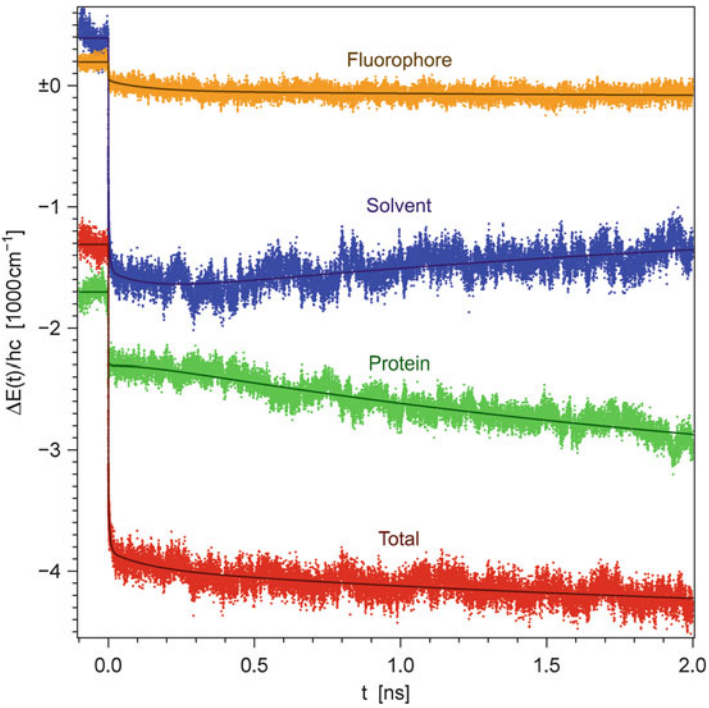

Fig. 2.5 TDSS obtained using the direct-response method, ensemble-averaged over 100 trajectories. Different colors are used to depict the total TDSS (*red*), the solvent contribution to TDSS (*blue*), the contribution from all protein atoms, including fluorophore (*green*), and the contribution from the fluorophore only (*orange*). *Dots* represent the ensemble mean values of $\Delta E(t)/hc$, *solid lines* represent the best global fits by the multiexponential model function from Eq. (2.50) with $N_{exp} = 5$. Reprinted with permission from Ref. [62], copyright 2010 American Chemical Society

pairwise distances between the α-carbons of the protein amino-acids were calculated from each of the 100 trajectories and then ensemble-averaged. The resulting functions of time were fit by the model function from Eq. (2.50) with the fixed values of the five relaxation times τ_n (the values had been obtained in the global fitting of the component TDSS). The amplitudes $\alpha_{c,n}$ (where the subscript c now represents the serial number of the internal coordinate or distance between α-carbons) and the standard deviations of these amplitudes were screened to detect those amplitudes that were statistically significant (i. e., the absolute value of the amplitude exceeds the standard deviation at least threefold). This gave an idea which internal coordinates or distances between α-carbons change in correlation with each of the five relaxation modes. The results are listed below.

On the time scale of $\tau_1 = 36.1$ fs there were significant changes in the bond angles and dihedral angles of several groups in close proximity to the fluorophore, for example, the backbone NH group of Trp-43 (the very residue whose sidechain plays the role of the fluorophore) and the backbone CO group of Gly-41, which is

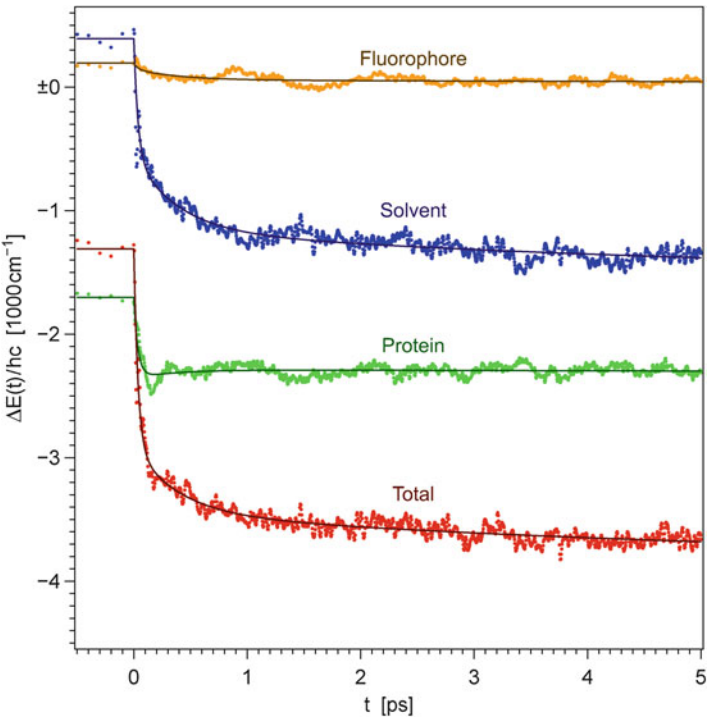

Fig. 2.6 Direct-response TDSS data from Fig. 2.5, shown on a 400-fold expanded time scale to reveal the early stages of the relaxation process. The color scheme and the roles of the *dots* and *solid lines* are the same as in Fig. 2.5. Reprinted with permission from Ref. [62], copyright 2010 American Chemical Society

only about 3 Å away from the fluorophore. The systematic changes in the bond angles and dihedral angles of these groups in close proximity to the fluorophore are quite small, but they still contribute about 656 cm^{-1} or 1.87 kcal/mol to the TDSS on this ultrafast time scale. Slightly more than that (944 cm^{-1} or 2.70 kcal/mol) is contributed by the librational relaxation of water molecules. The librational relaxation mode involves very small adjustments in the orientations of the solvent molecules, which do not result in breaking of the hydrogen bonds. This type of relaxation was observed both in the experiment [18] and in MD simulations [64]; the time scale of this solvent relaxation mode is usually faster than 50 fs.

On the time scale of $\tau_2 = 384$ fs and $\tau_3 = 5.63$ ps none of the protein internal coordinates or distances between α-carbons undergo statistically significant changes. Furthermore, as it can be clearly seen in Fig. 2.7, neither the motion of protein atoms nor the motion of the fluorophore significantly contributes to the second and the third relaxation component. These relaxation components represent two modes of solvent relaxation. We already know that for real water $\tau_L = 550$ fs and $\tau_D = 8.3$ ps. The value of τ_2 from MD simulations is 30 % shorter than the experimental value of τ_L and the value of τ_3 from MD simulations is 30 % shorter

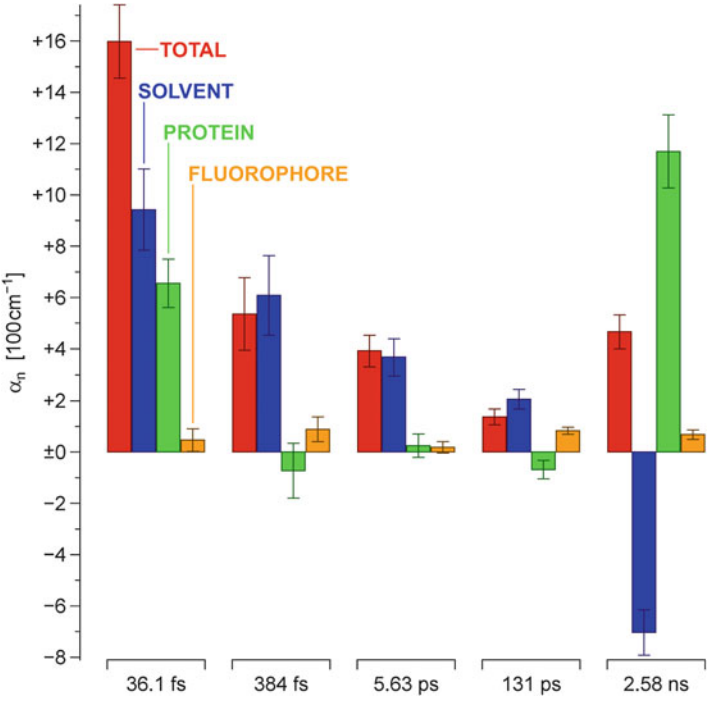

Fig. 2.7 A histogram of the amplitudes corresponding to the five exponential terms recovered in the global fitting of the direct-response TDSS data by the model function in Eq. (2.50). *Red color* denotes the total amplitude α_n. *Blue color* denotes the solvent contribution $\alpha_{s,n}$. *Green color* denotes the protein contribution $\alpha_{p,n}$. *Orange color* denotes the fluorophore contribution $\alpha_{f,n}$. *Error bars* represent 95 % confidence intervals. Corresponding values of τ_n are shown at the bottom. Reprinted with permission from Ref. [62], copyright 2010 American Chemical Society

than the experimental value of τ_D. This is a well-known artifact of TIP3P water model, which was used in the MD simulations described here [62]. In a hybrid QM-MD simulations of 3-methylindole in TIP3P water [64] the longitudinal relaxation time was found to be 400 fs, which is also about 30 % less than the experimental value of τ_D. All this points to the fact that the second and the third relaxation component represent the longitudinal and the transverse relaxation modes of bulk water, with the amplitudes of 536 cm^{-1} or 1.53 kcal/mol and 393 cm^{-1} or 1.12 kcal/mol, respectively.

On the time scale of $\tau_4 = 131$ ps statistically significant but modest changes (not exceeding 3°) in the ensemble mean values of some backbone dihedral angles ϕ and ψ are observed on the time scale of τ_4, and most of these changes are observed in the turn regions, residues 9–12, 20–23, and 36–42, see Fig. 2.8. This indicates that the secondary-structure elements (one α-helix and four β-strands) do not change their conformation, but an adjustment of the tertiary structure takes place on the time scale of τ_4. The nature of this adjustment becomes clear when we look at the changes in the distance between the α-carbon of each residue and the α-carbon of

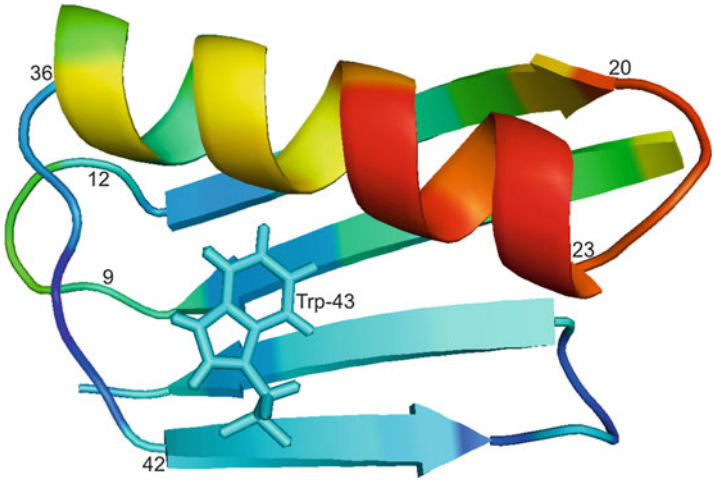

Fig. 2.8 Representative relaxed excited-state structure of GB1, depicted using cartoon representation in PyMOL [80]. The color represents the change in the ensemble mean distance between the α-carbon of each residue and the α-carbon of Trp-43 that takes place on the time scale of the relaxation component τ_4. A residue that does not move closer or further away from Trp-43 is depicted by *cyan color*. The residues that move away from Trp-43 are depicted by *green*, *yellow*, *orange*, and *red colors*, with the *red color* corresponding to the largest positive change in the distance (about +0.23 Å) on the time scale of τ_4. The residues that move closer to Trp-43 are depicted by the shades of *blue color*, with the *dark blue color* corresponding to the largest negative change in the distance (about −0.06 Å) on the time scale of τ_4. Reprinted with permission from Ref. [62], copyright 2010 American Chemical Society

Trp-43. The time scale of τ_4 is the only time scale on which the changes in the distances between α-carbons are statistically significant. On the time scales of τ_1, τ_2, τ_3, and τ_5 there is no statistically-significant changes in distances between α-carbons. As it can be clearly seen from Fig. 2.8, on the time scale of τ_4 the α-helix pulls away from the β-strand containing Trp-43, and this allows a slightly greater water access to the fluorophore. Note, that all the energy of the red shift comes from water, which contributes 206 cm^{-1} or 0.59 kcal/mol, whereas the contribution of the protein equals −69 cm^{-1} or −0.20 kcal/mol (the negative amplitude corresponds to the blue shift). There is a negative correlation between the contributions from the solvent and the protein on the time scale of τ_4. Although the interaction between the solvent and the fluorophore provides all the energy for the motion on this time scale, the relaxation process on the time scale of τ_4 reflects the protein dynamics, specifically the dynamics of small adjustments in the tertiary structure. This shows that the conclusions based solely on the energy contributions to TDSS from the protein atoms and solvent atoms can be misleading.

On the time scale of $\tau_5 = 2.58$ ns statistically significant changes are observed in the dihedral angles χ_1 and χ_2 of Glu-42 sidechain. The nature of these changes becomes obvious from Fig. 2.9, where each color point represents one Glu-42 sidechain conformation saved during the MD simulation described elsewhere

[62]. A total 2.1 million points, representing 100 MD trajectories are shown in Fig. 2.9. The color of each point is related to the time from the instance when the charges on the fluorophore (the Trp-43 sidechain) were changed from $Q_{j0}^{(0)}$ to $Q_{j1}^{(0)}$ (this time is taken for t=0). At t<0 the color is deep blue. During the time between 0 and 1 ns the color gradually shifts from blue to green. During the time between 1 and 2 ns the color gradually shifts from green to red. This makes it possible to see that the populations of the Glu-42 sidechain rotamers marked D and E in Fig. 2.9 are high in the ground state, but they decrease after the excitation of Trp-43. On the other hand, the populations of the Glu-42 sidechain rotamers marked C and H in Fig. 2.9 are low in the ground state and they increase after the excitation of Trp-43. In configurations C and H the negatively-charged $-CO_2^-$ group at the end of Glu-42 sidechain is very close to the positively-charged end of the excited-state fluorophore, which is not the case in configurations D and E. The conformational change of the Glu-42 sidechain results in a 1170 cm^{-1} or 3.33 kcal/mol contribution to the TDSS, which is opposed by the -703 cm^{-1} or -2.00 kcal/mol contribution from the solvent.

The negative contribution of water to the relaxation component τ_5 can be explained in terms of the dielectric continuum model [63]. If $\Delta E = 1170$ cm^{-1} is the energy contribution to TDSS from the motion of Glu-42 sidechain in vacuum, and if we neglect the physical dimensions of the Glu-42 sidechain as well as the fluorophore and the rest of the protein and consider the motion of point-charges immersed in continuous solvent of the dielectric constant ε_S, then in the solvent the TDSS amplitude will decrease from ΔE to $\Delta E/\varepsilon_S$, which means that the solvent contribution to the TDSS equals $\Delta E/\varepsilon_S - \Delta E$, and this is always a negative number. If we take $\varepsilon_S = 78.36$, then the solvent contribution to the TDSS estimated using the formula $\Delta E/\varepsilon_S - \Delta E$ equals -1155 cm^{-1}; the value actually obtained from the MD simulations is only -703 cm^{-1}. The difference in the magnitude shows that it was a crude approximation to neglect the physical dimensions of the Glu-42 sidechain as well as the fluorophore and the rest of the protein; in spite of this crude approximation the negative sign of the solvent contribution was explained correctly, at least on the qualitative level.

The net amplitude of the TDSS associated with the conformational change of the Glu-42 sidechain obtained from MD simulations equals 466 cm^{-1} [62]. The amplitude of the slow TDSS measured experimentally equals 706 cm^{-1} [41], however, the experimental amplitude should be compared to the sum of the amplitudes corresponding to τ_4 and τ_5 [41], which equals 603 cm^{-1}. The difference between 603 and 706 cm^{-1} is within experimental errors. The main problem is that the value of $\tau_5 = 2.58 \pm 1.06$ ns determined from MD simulations [62] is about 30-fold greater than the experimentally measured τ value of 77 ps [41]. Several explanations of this disagreement are possible. First, it is possible that in CHARMM the potential barriers separating different sidechain conformations are higher than in the real life. Second, it is possible that the sidechain can tunnel through the potential barrier like the nitrogen nucleus in NH_3 molecule can tunnel through the plane of the three hydrogen nuclei (see the description of the ammonia maser in the

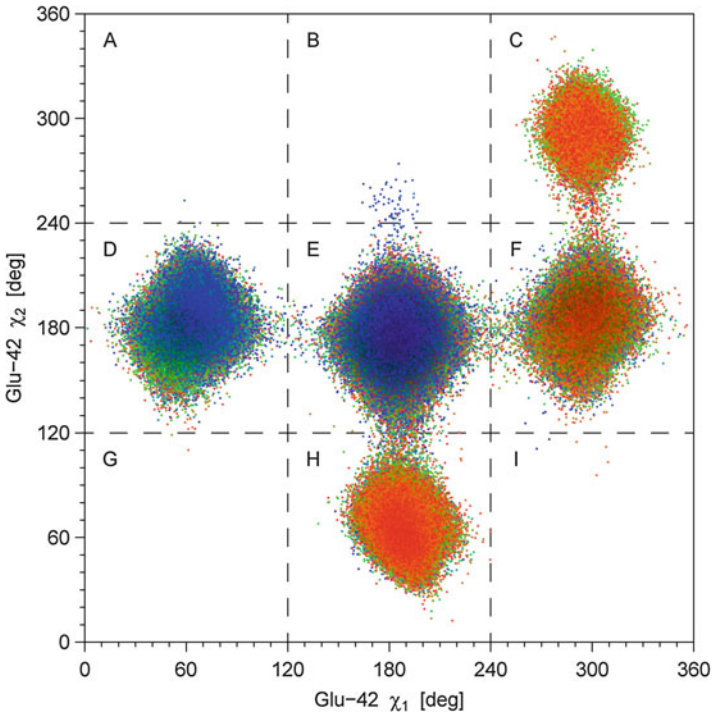

Fig. 2.9 The set of transient Glu-42 side chain conformations, depicted by $2.1 \cdot 10^6$ *color dots* on a plot of χ_2 versus χ_1. The internal coordinates (χ_1,χ_2) were saved at 0.1 ps intervals along 100 trajectories. The color of each dot is blue at early times (ground state and the early part of the excited-state trajectory). During the first 1 ns in the excited state the dot color gradually shifts from blue to green, and during the second 1 ns the color shifts from green to red. Overlaps between dots are colored using pigment mixing rules rather than intensity addition rules. Variable brightness enhancement prevents areas where too many dots of different colors overlap from going completely black. Broken lines divide the χ_1-χ_2 space into nine rotamers, labeled with letters A through I. Each rotamer represents a topologically connected area of high dot density on this plot. To prevent splitting of the connected areas at the artificial boundaries where $\chi_1 = \pm 180°$ or $\chi_2 = \pm 180°$, the angles χ_1 and χ_2 have been redefined so that their domain is $0° \leq \chi < 360°$ rather than $-180° < \chi \leq 180°$. Reprinted with permission from Ref. [62], copyright 2010 American Chemical Society

introduction to this chapter). Finally, it is possible that in the 77 ps relaxation time observed in the experiment describes the relaxation of the counter-ions (such as K^+) that are likely to be found near the $-CO_2^-$ group, but were not included in the MD simulation [62]. The hypothesis regarding counter-ions can be verified experimentally by running the experiments in solvents containing different ions (Li^+ or Na^+ instead of K^+), of different ionic strengths, and of different pH. If the slow relaxation rate or the TDSS amplitude associated with it varies with any of these experimental parameters, then this will show that the TDSS can detect the motion of counterions near charged groups on protein surfaces.

2.11 Conclusions

The TDSS in fluorescence emission of tryptophan residues in proteins can be utilized to obtain valuable information regarding protein dynamics in the frequency range between 300 MHz and 300 GHz, where non-optical experimental methods cannot provide sufficient information. This chapter describes how the results obtained in the experimental studies can be interpreted using computer MD simulations. It has been shown how the experimentally-observed TDSS curves can be obtained theoretically from MD simulations, how the simulated TDSS curves can be separated into multiple relaxation modes, and how the physical nature of the motions associated with each relaxation mode can be identified. Two relaxation modes for the bulk solvent have been described, one of which can be observed only if the protein contains internal water channels or pockets. The methods described in this chapter can be used to study the dynamics of soft vibration modes in proteins as well as the dynamics of internal water molecules in the protein core and the motions of counterions near the protein surface.

Acknowledgments This research was supported by the National Science Foundation awards MCB-0719248 and MCB-1051996.

References

1. Cornell WD, Cieplak P, Bayly CI, Gould IR, Merz KM Jr, Ferguson DM, Spellmeyer DC, Fox T, Caldwell JW, Kollman PAJ (1995) A second generation force field for the simulation of proteins, nucleic acids, and organic molecules. Am Chem Soc 117:5179–5197
2. MacKerell AD Jr, Bashford D, Bellott M, Dunbrack RL Jr, Evanseck J, Field MJ, Fischer S, Gao J, Guo H, Ha S, Joseph D, Kuchnir L, Kuczera K, Lau FTK, Mattos C, Michnick S, Ngo T, Nguyen DT, Prodhom B, Reiher IWE, Roux B, Schlenkrich M, Smith J, Stote R, Straub J, Watanabe M, Wiorkiewicz-Kuczera J, Yin D, Karplus M (1998) All-hydrogen empirical potential for molecular modeling and dynamics studies of proteins using the CHARMM22 force field. J Phys Chem B 102:3586–3616
3. Scott WRP, Huenenberger PH, Tironi IG, Mark AE, Billeter SR, Fennen J, Torda AE, Huber T, Krueger P, van Gunsteren WF (1999) The GROMOS biomolecular simulation program package. J Phys Chem A 103:3596–3607
4. Palmer AG III (2001) NMR probes of molecular dynamics: overview and comparison with other techniques. Annu Rev Biophys Biomol Struct 30:129–155
5. Banyai DR, Murakhtina T, Sebastiani D (2010) NMR chemical shifts as a tool to analyze first principles molecular dynamics simulations in condensed phases: the case of liquid water. Magn Reson Chem 48:S56–S60
6. Parkesh R, Fountain M, Disney MD (2011) NMR spectroscopy and molecular dynamics simulation of r(CCGCUGCGG)$_2$ reveal a dynamic UU internal loop found in myotonic dystrophy type 1. Biochemistry 50:599–601
7. Fersht AR, Daggett V (2002) Protein folding and unfolding at atomic resolution. Cell 108:1–20

8. Scheraga HA, Khalili M, Liwo A (2007) Protein-folding dynamics: overview of molecular simulation techniques. Annu Rev Phys Chem 58:57–83
9. Bolhuis PG (2009) Two-state protein folding kinetics through all-atom molecular dynamics based sampling. Front Biosci 14:2801–2828
10. Deng Y, Roux BJ (2009) Computations of standard binding free energies with molecular dynamics simulations. Phys Chem B 113:2234–2246
11. Landau LD, Lifschitz EM (1977) Quantum mechanics (non-relativistic theory), 3rd edn. Pergamon Press, Oxford
12. Gordon JP, Zeiger HJ, Townes CH (1955) The maser – New type of microwave amplifier, frequency standard, and spectrometer. Phys Rev 99:1264–1274
13. Gordon JP, Zeiger HJ, Townes CH (1954) Molecular microwave oscillator and new hyperfine structure in the microwave spectrum of NH_3. Phys Rev 95:282–284
14. Dennison DM, Uhlenbeck GE (1932) The two-minima problem and the ammonia molecule. Phys Rev 41:313–321
15. Rosen N, Morse PM (1932) On the vibrations of polyatomic molecules. Phys Rev 42:210–217
16. Ware WR, Chow P, Lee SK (1968) Time-resolved nanosecond emission spectroscopy: spectral shifts due to solvent-solute relaxation. Chem Phys Lett 2:356–358
17. Maroncelli M (1993) The dynamics of solvation in polar liquids. J Mol Liq 57:1–37
18. Jimenez R, Fleming GR, Kumar PV, Maroncelli M (1994) Femtosecond solvation dynamics of water. Nature 369:471–473
19. Horng ML, Gardecki JA, Papazyan A, Maroncelli M (1995) Subpicosecond measurements of polar solvation dynamics: Coumarin 153 revisited. J Phys Chem 99:17311–17337
20. Stratt RM, Maroncelli M (1996) Nonreactive dynamics in solution: the emerging molecular view of solvation dynamics and vibrational relaxation. J Phys Chem 100:12981–12996
21. Gardecki JA, Maroncelli M (1999) Comparison of the single-wavelength and spectral-reconstruction methods for determining the solvation-response function. J Phys Chem A 103:1187–1197
22. Kovalenko SA, Schanz R, Senyushkina TA, Ernsting NP (2002) Femtosecond spectroscopy of *P*-dimethylaminocyanostilbene in solution No evidence for dual fluorescence. Phys Chem Chem Phys 4:703–707
23. Arzhantsev S, Jin H, Baker GA, Maroncelli M (2007) Measurements of the complete solvation response in ionic liquids. J Phys Chem B 111:4978–4989
24. Sajadi M, Obernhuber T, Kovalenko SA, Mosquera M, Dick B, Ernsting NP (2009) Dynamic polar solvation is reported by fluorescing 4-aminophthalimide faithfully despite H-bonding. J Phys Chem A 113:44–55
25. Brand L, Gohlke JR (1971) Nanosecond time-resolved fluorescence spectra of a protein-dye complex. J Biol Chem 246:2317–2324
26. Gafni A, DeToma RP, Manrow RE, Brand L (1977) Nanosecond decay studies of a fluorescence probe bound to apomyoglobin. Biophys J 17:155–168
27. Pierce DW, Boxer SG (1992) Dielectric relaxation in a protein matrix. J Phys Chem 96:5560–5566
28. Riter RR, Edington MD, Beck WF (1996) Protein-matrix solvation dynamics in the α subunit of *C*-phycocyanin. J Phys Chem 100:14198–14205
29. Jordanides XJ, Lang MJ, Song X, Fleming GR (1999) Solvation dynamics in protein environments studied by photon echo spectroscopy. J Phys Chem B 103:7995–8005
30. Changenet-Barret P, Choma CT, Gooding EF, DeGrado WF, Hochstrasser RM (2000) Ultrafast dielectric response of proteins from dynamics stokes shifting of coumarin in calmodulin. J Phys Chem B 104:9322–9329
31. Vincent M, Gilles AM, de la Sierra IML, Briozzo P, Barzu O, Gallay J (2000) Nanosecond fluorescence dynamic stokes shift of tryptophan in a protein matrix. J Phys Chem B 104:11286–11295

32. Pal SK, Mandal D, Sukul D, Sen S, Bhattacharyya K (2001) Solvation dynamics of DCM in human serum albumin. J Phys Chem B 105:1438–1441
33. Toptygin D, Savtchenko RS, Meadow ND, Brand L (2001) Homogeneous spectrally- and time-resolved fluorescence emission from single-tryptophan mutants of IIAGlc protein. J Phys Chem B 105:2043–2055
34. Cohen BE, McAnaney TB, Park ES, Jan YN, Boxer SG, Jan LY (2002) Probing protein electrostatics with a synthetic fluorescent amino acid. Science 296:1700–1703
35. Pal SK, Peon J, Bagchi B, Zewail AH (2002) Biological water: femtosecond dynamics of macromolecular hydration. J Phys Chem B 106:12376–12395
36. Peon J, Pal SK, Zewail AH (2002) Hydration at the surface of the protein monellin: dynamics with femtosecond resolution. Proc Natl Acad Sci U S A 99:10964–10969
37. Mataga N, Chosrowjan H, Taniguchi S, Hamada N, Tokunaga F, Imamoto Y, Kataoka M (2003) Ultrafast photoreactions in protein nanospaces as revealed by fs fluorescence dynamics measurements on photoactive yellow protein and related systems. Phys Chem Chem Phys 5:2454–2460
38. Lampa-Pastirk S, Beck WF (2004) Polar solvation dynamics in Zn(II)-substituted cytochrome *C*: diffusive sampling of the energy landscape in the hydrophobic core and solvent-contact layer. J Phys Chem B 108:16288–16294
39. Qiu W, Zhang L, Kao Y-T, Lu W, Li T, Kim J, Sollenberger GM, Wang L, Zhong D (2005) Ultrafast hydration dynamics in melittin folding and aggregation: helix formation and tetramer self-assembly. J Phys Chem B 109:16901–16910
40. Guha S, Sahu K, Roy D, Mondal SK, Roy S, Bhattacharyya K (2005) Slow solvation dynamics at the active site of an enzyme: implications for catalysis. Biochemistry 44:8940–8947
41. Toptygin D, Gronenborn AM, Brand L (2006) Nanosecond relaxation dynamics of protein GB1 identified by the time-dependent Red shift in the fluorescence of tryptophan and 5-fluorotryptophan. J Phys Chem B 110:26292–26302
42. Qiu WH, Kao YT, Zhang LY, Yang Y, Wang LJ, Stites WE, Zhong DP, Zewail AH (2006) Protein surface hydration mapped by site-specific mutations. Proc Natl Acad Sci U S A 103:13979–13984
43. Abbyad P, Shi XH, Childs W, McAnaney TB, Cohen BE, Boxer SG (2007) Measurement of solvation responses at multiple sites in a globular protein. J Phys Chem B 111:8269–8276
44. Halder M, Mukherjee P, Bose S, Hargrove MS, Song XY, Petrich JW (2007) Solvation dynamics in protein environments: comparison of fluorescence upconversion measurements of Coumarin 153 in monomeric hemeproteins with molecular dynamics simulations. J Chem Phys 127:055101
45. Li T, Hassanali AA, Kao Y-T, Zhong D, Singer SJ (2007) Hydration dynamics and time scales of coupled water-protein fluctuations. J Am Chem Soc 129:3376–3382
46. Zhang L, Wang L, Kao Y-T, Qiu W, Yang Y, Okobiah O, Zhong D (2007) Mapping hydration dynamics around a protein surface. Proc Natl Acad Sci U S A 104:18461–18466
47. Abbyad P, Childs W, Shi X, Boxer SG (2007) Dynamic stokes shift in green fluorescent protein variants. Proc Natl Acad Sci U S A 104:20189–20194
48. Jesenska A, Sykora J, Olzynska A, Brezovsky J, Zdrahal Z, Damborsky J, Hof M (2009) Nanosecond time-dependent stokes shift at the tunnel mouth of haloalkane dehalogenases. J Am Chem Soc 131:494–501
49. Zhang LY, Yang Y, Kao YT, Wang LJ, Zhong DP (2009) Protein hydration dynamics and molecular mechanism of coupled water-protein fluctuations. J Am Chem Soc 131:10677–10691
50. Othon CM, Kwon OH, Lin MM, Zewail AH (2009) Solvation in protein (un)folding of melittin tetramer-monomer transition. Proc Natl Acad Sci U S A 106:12593–12598
51. Kwon O-H, Yoo TH, Othon CM, Van Deventer JA, Tirrell DA, Zewail AH (2010) Hydration dynamics at fluorinated protein surfaces. Proc Natl Acad Sci U S A 107:17101–17106
52. Zhong D, Pal SK, Zewail AH (2011) Biological water: a critique. Chem Phys Lett 503:1–11

53. Brauns EB, Madaras ML, Coleman RS, Murphy CJ, Berg MA (1999) Measurement of local DNA reorganization on the picosecond and nanosecond time scales. J Am Chem Soc 121:11644–11649
54. Andreatta D, Lustres JLP, Kovalenko SA, Ernsting NP, Murphy CJ, Coleman RS, Berg MA (2005) Power-law solvation dynamics in DNA over six decades in time. J Am Chem Soc 127:7270–7271
55. Callis PR, Burgess BK (1997) Tryptophan fluorescence shifts in proteins from hybrid simulations: an electrostatic approach. J Phys Chem B 101:9429–9432
56. Vivian JT, Callis PR (2001) Mechanisms of tryptophan fluorescence shifts in proteins. Biophys J 80:2093–2109
57. Nilsson L, Halle B (2005) Molecular origin of time-dependent fluorescence shifts in proteins. Proc Natl Acad Sci U S A 102:13867–13872
58. Bandyopadhyay S, Chakraborty S, Balasubramanian S, Bagchi B (2005) Sensitivity of polar solvation dynamics to the secondary structures of aqueous proteins and the role of surface exposure of the probe. J Am Chem Soc 127:4071–4075
59. Hassanali AA, Li TP, Zhong DP, Singer SJ (2006) A molecular dynamics study of Lys-Trp-Lys: structure and dynamics in solution following photoexcitation. J Phys Chem B 110:10497–10508
60. Golosov AA, Karplus M (2007) Probing polar solvation dynamics in proteins: a molecular dynamics simulation analysis. J Phys Chem B 111:1482–1490
61. Li T, Hassanali AA, Singer SJ (2008) Origin of slow relaxation following photoexcitation of W7 in myoglobin and the dynamics of its hydration layer. J Phys Chem B 112:16121–16134
62. Toptygin D, Woolf TB, Brand L (2010) Picosecond protein dynamics: the origin of the time-dependent spectral shift in the fluorescence of the single Trp in the protein GB1. J Chem Phys B 114:11323–11337
63. Halle B, Nilsson L (2009) Does the dynamic stokes shift report on slow protein hydration dynamics? J Phys Chem B 113:8210–8213
64. Muino PL, Callis PR (1994) Hybrid simulations of solvation effects on electronic spectra: indoles in water. J Chem Phys 100:4093–4109
65. Toptygin D, Brand L (2000) Spectrally- and time-resolved fluorescence emission of indole during solvent relaxation: a quantitative model. Chem Phys Lett 322:496–502
66. We use bold typeface **E** to denote the electric field vector and light typeface italic *E* to denote energy. To avoid confusion, the magnitude of vector **E** is denoted as |**E**| rather than *E*
67. In this context the term "mean" implies averaging of the three Cartesian components of the electric field vector in the reference frame that rotates together with the fluorophore
68. Mulliken RS (1955) Electronic population analysis on LCAO-MO molecular wave functions. J Chem Phys 23:1833–1840
69. Callis PR (1991) Molecular orbital theory of the ^1L_b and ^1L_a states of indole. J Chem Phys 95:4230–4240
70. Pan C-P, Callis PR, Barkley MD (2006) Dependence of tryptophan emission wavelength on conformation in cyclic hexapeptides. J Phys Chem B 110:7009–7016
71. Landau LD, Lifschitz EM (1976) Mechanics, 3rd edn. Pergamon Press, Oxford
72. Maroncelli M, Fleming GR (1988) Computer simulation of the dynamics of aqueous solvation. J Chem Phys 89:5044–5069
73. Hubbard J, Onsager L (1977) Dielectric dispersion and dielectric friction in electrolyte solutions. J Chem Phys 67:4850–4857
74. Maroncelli M, Fleming GR (1987) Picosecond solvation dynamics of Coumarin 153: the importance of molecular aspects of solvation. J Chem Phys 86:6221–6239
75. Castner EW, Fleming GR, Bagchi B, Maroncelli M (1988) The dynamics of polar solvation: inhomogeneous dielectric continuum models. J Chem Phys 89:3519–3534
76. Kivelson D, Friedman H (1989) Longitudinal dielectric relaxation. J Phys Chem 93:7026–7031
77. Kaatze U (1993) Dielectric relaxation of H_2O/D_2O mixtures. Chem Phys Lett 203:1–4

78. Martinez SE, Huang D, Ponomarev M, Cramer WA, Smith JL (1996) The heme redox center of chloroplast cytochrome *F* is linked to a buried five-water chain. Protein Sci 5:1081–1092
79. Pomès R, Roux B (1998) Free energy profiles for H^+ conduction along hydrogen-bonded chains of water molecules. Biophys J 75:33–40
80. DeLano W (2009) Pymol home page. www.pymol.org

http://www.springer.com/978-3-319-24607-9

Reviews in Fluorescence 2015
Geddes, C.D. (Ed.)
2016, VIII, 380 p. 152 illus., 91 illus. in color., Hardcover
ISBN: 978-3-319-24607-9